Hemozoin produced by mammals confers heme tolerance

Rini H. Pek[1], Xiaojing Yuan[1], Nicole Rietzschel[1], Jianbing Zhang[1], Laurie K. Jackson[2], Eiji Nishibori[3], Ana Ribeiro[1], William R. Simmons[5], Jaya Jagadeesh[5], Hiroshi Sugimoto[6], Md Zahidul Alam[7], Lisa J. Garrett[4], Malay Haldar[7], Martina Ralle[8], John Phillips[2], David Bodine[4], and Iqbal Hamza[1*]

[1]*Department of Animal & Avian Sciences and Department of Cell Biology & Molecular Genetics, University of Maryland, College Park, MD, USA*
[2]*Department of Medicine, University of Utah School of Medicine, Salt Lake City, UT, USA*
[3]*Faculty of Pure and Applied Sciences and Tsukuba Research Center for Energy Materials Science (TREMS), University of Tsukuba, Tsukuba, 305-8571, Japan.*
[4]*NHGRI embryonic Stem Cell and Transgenic Mouse Core, National Human Genome Research Institute, National Institutes of Health, Bethesda, MD, USA*
[5]*Genetics and Molecular Biology Branch, National Human Genome Research Institute, National Institutes of Health, Bethesda, MD, USA*
[6]*RIKEN SPring-8 Center, Sayo, 679-5148, Japan*
[7]*Department of Pathology and Laboratory Medicine, Perelman School of Medicine at the University of Pennsylvania , Philadelphia, PA, USA.*
[8]*Department of Molecular and Medical Genetics, Oregon Health and Science University, Portland, OR, USA*

*To whom correspondence should be addressed.

Iqbal Hamza, Ph.D.
University of Maryland, College Park
2413 ANSC, Bldg 142
College Park, Maryland 20742
Phone: 301-405-0649
Fax: 301-405-7980
Email: hamza@umd.edu

ABSTRACT

Free heme is cytotoxic as exemplified by hemolytic diseases and genetic deficiencies in heme recycling and detoxifying pathways. Thus, intracellular accumulation of heme has not been observed in mammalian cells to date. Here we show that mice deficient for the heme transporter HRG1 accumulate over ten-fold excess heme in reticuloendothelial macrophage lysosomes that are 10 to 100 times larger than normal. Macrophages tolerate these high concentrations of heme by polymerizing them into crystalline hemozoin, which heretofore has only been found in blood-feeding parasites. *HRG1* deficiency results in impaired erythroid maturation and an inability to systemically respond to iron deficiency. Complete heme tolerance requires a fully-operational heme degradation pathway as haploinsufficiency of *HMOX1* combined with *HRG1* inactivation causes perinatal lethality demonstrating synthetic lethal interactions between heme transport and degradation. Our studies establish the formation of hemozoin by mammals as a previously unsuspected heme tolerance pathway.

INTRODUCTION.

Hemolysis can arise from genetic mutations (Larsen et al., 2012), parasitic and bacterial infections (Orf and Cunnington, 2015), and drug-induced autoimmune reactions (Garratty, 2009). Rupturing of red blood cells (RBCs) releases high concentrations of heme, which promotes reactive oxygen species (ROS) production (Fibach and Rachmilewitz, 2008) and inflammation (Dutra et al., 2014) causing tissue damage and death. Consistent with the cytotoxicity of heme, genetic ablation of the heme degrading enzyme, heme oxygenase 1 (HMOX1), results in >90% embryonic lethality (Kovtunovych et al., 2010; Poss and Tonegawa, 1997a, b). The few mice that survive are susceptible to hemolytic infections (Seixas et al., 2009), and have little or no reticuloendothelial macrophages (Kovtunovych et al., 2010), a phenotype attributed to heme cytotoxicity.

The majority of body heme is encapsulated within RBCs, and each RBC contains over one billion heme molecules. As RBCs undergo senescence or become damaged, they are engulfed by macrophages from the reticuloendothelial system (RES) through a process termed erythrophagocytosis (EP) (Ganz, 2012; Ganz and Nemeth, 2006; Klei et al., 2017; Winter et al., 2014). As RBCs contain both heme and non-heme iron, transporters for each metabolite are recruited to the erythrophagosomal membranes (Delaby et al., 2012; Soe-Lin et al., 2010). The heme responsive gene-1 (HRG1/SLC48A1) transports heme from the erythrophagosome into the cytosol (Rajagopal et al., 2008; White et al., 2013). Heme is enzymatically degraded by HMOX1 (Kovtunovych et al., 2010; Kovtunovych et al., 2014) to liberate iron, which can either be stored in ferritin (FTH1) or exported out of the cell by ferroportin (FPN1) to be reutilized for new RBC production (Knutson et al., 2005; Knutson et al., 2003), including developing erythroblasts in the bone marrow (Raja et al., 1999). Excess heme is exported from the cell by

feline leukemia virus subgroup C cellular receptor 1 (FLVCR1) to prevent heme toxicity (Keel et al., 2008). Consequently, genetic disruption in *HMOX1*, *FPN1*, *FTH1*, and *FLVCR1* - steps in the heme-iron recycling pathway - causes embryonic lethality in mice. Here, we show that mice lacking the heme transporter *HRG1* are viable despite accumulating high concentrations of heme. These animals are heme tolerant because they sequester heme within enlarged lysosomes in the RES macrophages and polymerize them into hemozoin, which heretofore has only been found in blood-feeding parasites (Shio et al., 2010; Toh et al., 2010). Our work suggests the existence of a previously unknown pathway for heme detoxification and tolerance in mammals.

RESULTS

Reticuloendothelial tissues accumulate dark pigments in the absence of *HRG1*

To uncover the *in vivo* function of HRG1 in mammals, we generated *HRG1*-deficient mice using CRISPR/Cas9 gene editing. Guide RNAs targeting exon 1 of mouse *HRG1* (**Fig. 1A)** produced seven mutant alleles in C57BL/6 x 129/SvJ F_1 animals (**Supplemental Table 1)** which were backcrossed to C57BL/6 mice before intercrossing. We observed similar phenotypes in all mutant alleles and focused on the M6 allele which contains a two base-pair deletion in exon 1 of *HRG1* (M6). This deletion causes a frameshift within the thirty-third codon immediately after the first transmembrane domain (**Fig. 1B; Supplemental Fig. 1A)**. Intercrossing *HRG1*$^{+/-}$ animals produced *HRG1*$^{-/-}$ animals with the expected Mendelian ratio (**Supplemental Fig. 1B)**. While *HRG1* mRNA was still detected (not shown), immunoblots and immunohistochemistry of *HRG1*$^{-/-}$ RES tissues showed no detectable HRG1 protein, compared to *HRG1*$^{+/+}$ tissues which express abundant HRG1 (**Fig. 1C, D)**. *HRG1*$^{-/-}$ mice had significantly larger spleens and lower hematocrits (**Fig. 1E, F)**. Gross morphological examination of six-week old *HRG1*$^{-/-}$ mice

revealed darkened spleen, bone marrow, and liver (**Fig. 1G)** that corresponded with dark intracellular pigments in histochemical tissue sections (**Fig. 1D, right panel)**.

HRG1$^{-/-}$ mice exhibit extramedullary erythropoiesis with fewer mature RPMs

An enlarged spleen is a common hallmark of ineffective and stress erythropoiesis (Lenox et al., 2005; Perry et al., 2009) . We therefore investigated the erythroid compartment of bone marrows and spleens of these mice using Ter-119 and CD44 markers to follow erythroid differentiation and proliferation (Chen et al., 2009). Consistent with the reduced hematocrits, *HRG1*$^{-/-}$ mice had fewer total Ter-119^{+} cells in the bone marrow but more basophilic erythroblasts (population II) which are symptomatic of an impairment in erythroid maturation (**Fig. 2A-C; Supplemental Fig. 2A)**. In the spleen, despite similar numbers of total Ter-119^{+} cells (**Fig. 2D, E)**, *HRG1*$^{-/-}$ animals showed significantly more immature erythroid precursor cells (population II+III), suggesting compensatory erythropoiesis in the spleen (**Fig. 2D-F; Supplemental Fig. 2B)**.

Since *HRG1* is primarily expressed in RES macrophages (White et al., 2013), we analyzed red pulp macrophages (RPMs), which are the primary iron-recycling macrophages in the spleen (Beaumont and Delaby, 2009; Ganz, 2012; Haldar et al., 2014). Significantly fewer mature RPMs (F4/80^{hi}Treml4^{+}) were detected in *HRG1*$^{-/-}$ spleens (**Fig. 2G, H; Supplemental Fig. 2C)** which correlated with increased numbers of immature RPMs by ratiometric quantification of monocytes (F4/80^{int} : F4/80^{lo}-CD11b^{hi}) (**Fig. 2I, J; Supplemental Fig. 2D)**.

Heme accumulates within RES macrophages of *HRG1*$^{-/-}$ mice

HRG1$^{-/-}$ mice on a standard diet (380 ppm Fe) have normal serum iron, total iron binding capacity (TIBC) and transferrin saturation but significantly elevated serum ferritin, an indicator

of tissue iron-overload (Ganz and Nemeth, 2012) (**Supplemental Table 2)**. Histological analysis by H&E staining showed dark pigmented inclusions accumulating within RES organs of *HRG1*$^{-/-}$ mice **(Fig. 3A, right panel)**. However, *in situ* Perls' Prussian blue staining did not show significant differences in iron deposition in tissue biopsies (**Fig. 3B)**. Because it is possible that the dark pigments masked the visualization of the Prussian blue iron complex, we performed inductively coupled plasma mass spectrometry (ICP-MS) to measure total metal content. Significantly more iron was found in the spleens, livers and bone marrows of *HRG1*$^{-/-}$ mice (**Fig. 3C**), as compared to copper, zinc, and manganese (**Supplemental Fig. 3A-D)**; a modest 0.4-fold increase in manganese was observed in the spleens of *HRG1*$^{-/-}$ mice in contrast to 2-fold increase in iron (**Supplemental Fig. 3D)**. Differences in total metal content were also detected in other organs analyzed (**Supplemental Fig. 3A-D)**. These results show that *HRG1*$^{-/-}$ mice accumulate tissue iron that is not detectable by Prussian blue staining. Through a combination of ultra-performance liquid chromatography (UPLC) (Sinclair et al., 2001) and ICP-MS to measure heme-iron and total iron, we observed that *HRG1*$^{-/-}$ spleens and bone marrows had significantly more total heme (10-fold and 3-fold, respectively) than *HRG1*$^{+/+}$ organs (**Fig. 3D, Supplemental Fig. 3E)**, which indicates that the higher iron content observed in these tissues is due to the accumulation of heme.

We next sought to determine the identity of the cells containing the dark pigments. Immunohistochemistry using a macrophage-specific antibody showed dark inclusions in F4/80^{+} cells in all three RES tissues (**Fig. 3E, right panel arrows, Supplemental Fig. 3F-H)**. To spatially resolve the metal content at the subcellular level, we employed synchrotron-based X-ray fluorescence microscopy (XFM) which provides quantitative information about elemental distribution at the nanoscale. F4/80^{+} macrophages were isolated from the bone marrow by

magnetic bead separation, seeded on an appropriate sample support and visualized using XFM (Chen et al., 2015; Vogt, 2003). Overall, *HRG1*$^{-/-}$ macrophages contained significantly higher concentrations of cellular iron (**Fig. 3F, G)**, copper, sulfur, and calcium (**Fig. 3G)**. However, region-of-interest (ROI) quantification around the dark pigments in *HRG1*$^{-/-}$ macrophages confirmed that iron was the most abundant trace element within this region (**Fig. 3H)**.

Dietary iron deficiency disrupts iron metabolism gene expression in *HRG1*$^{-/-}$ mice and results in lethality

Total body iron is a composite of recycled heme-iron from damaged RBCs and dietary iron absorption. Since heme-iron accumulates within *HRG1*$^{-/-}$ macrophages which facilitate iron recycling during RBC turnover, we hypothesized that *HRG1*$^{-/-}$ mice might be more susceptible to a low-iron diet. The standard rodent diet contains ≈380 ppm of iron, which is significantly greater than the amount of iron (25 to 100 ppm) required to sustain normal erythropoiesis and the growth of laboratory mice (Sorbie and Valberg, 1974). We fed weanling *HRG1*$^{+/+}$ and *HRG1*$^{-/-}$ mice a low-iron diet (1.8 to 2 ppm Fe) and measured the impact of limiting dietary iron on their hematological indices. A significant percentage of *HRG1*$^{-/-}$ mice, but not *HRG1*$^{+/+}$ mice, died within 20 weeks on the low-iron diet (**Fig. 4A)**. Importantly, for the first five weeks, the hematocrits of *HRG1*$^{+/+}$ and *HRG1*$^{-/-}$ mice on the low-iron diet are comparable (Mazzaccara et al., 2008) (**Fig. 4B)**, but by eight weeks the hematocrits of *HRG1*$^{-/-}$ mice were significantly lower (p<0.01), and by 20 weeks they were severely anemic (13.2 ± 2.3 *HRG1*$^{-/-}$ versus 39.8 ± 2.2 *HRG1*$^{+/+}$, p<0.0001; **Fig. 4C**). These results imply that the defect in heme-iron recycling in *HRG1*$^{-/-}$ mice becomes more pronounced after five weeks on an iron-deficient diet. We therefore focused our subsequent analyses on mice that were on low-iron diets for five weeks to detect any molecular and physiological changes in the absence of overt hematological differences.

Analyses of serum from iron-deficient animals showed no significant differences in serum iron, TIBC, or transferrin saturation, but serum ferritin levels remained elevated in *HRG1*$^{-/-}$ mice on a low-iron diet (**Supplemental Table 2,** 2 ppm diet**)**. The levels of iron and heme retained within RES organs of *HRG1*$^{-/-}$ mice were also significantly higher than *HRG1*$^{+/+}$ mice (**Fig. 4D, E, Supplemental Fig 4A)**, suggesting that the heme-iron stores in *HRG1*$^{-/-}$ mice were not bioavailable despite systemic iron-deficiency.

In response to iron deficiency, the spleens of *HRG1*$^{+/+}$ mice increased by approximately 120% (**Fig. 4F)** (Lenox et al., 2005; Perry et al., 2009; Socolovsky, 2007), with a concomitant increase (7.5-fold) in immature Ter119^{+} cells, a hallmark of stress erythropoiesis (**Fig. 4G, H)**. In contrast, the stress erythropoiesis response in iron-deficient *HRG1*$^{-/-}$ mice was significantly attenuated (**Fig. 4F-H, Supplemental Fig. 4B)**, with erythroblast differentiation blocked at an earlier stage (population I) in the bone marrow (**Fig. 4I, Supplemental Fig. 4B-D)**. Iron deficiency fully restored the total numbers of mature RPM population and balance in monocyte populations (**Fig. 4J, K)** in *HRG1*$^{-/-}$ mice to wildtype levels (**Supplemental Fig. 4E, F)**. This could reflect increased viability of erythrophagocytic RPMs due to reduced heme accumulation in these cells under systemic iron deficiency.

To interrogate the responsiveness of iron and heme metabolism genes to iron deficiency in these mice, we assembled a custom qRT-PCR array comprising probes for 90 key iron/heme metabolism genes. Iron-deficient *HRG1*$^{-/-}$ mice showed significant dysregulation in 38% and 6% of these mRNAs in the spleen and liver, respectively (**Fig. 4L, Supplemental Fig. 4G-I, and Supplemental Table 3)**. Under iron deficient conditions, the levels of 32 iron metabolism mRNAs were significantly reduced in *HRG1*$^{+/+}$ spleens (**Supplemental Fig. 4H,** compare +/+ Standard vs +/+ 2 ppm, -/- Standard vs -/- 2 ppm**)**, but remained high in *HRG1*$^{-/-}$ spleens.

Together, these data suggest that *HRG1*$^{-/-}$ mice are unable to respond normally to iron-deficiency, especially at sites where heme-iron accumulates at high levels such as the spleen.

Loss of *HRG1* produces hemozoin biocrystals within enlarged lysosomes due to impaired erythrophagocytosis

To investigate the *in vivo* function of *HRG1* in heme-iron recycling, we labeled normal RBCs with ^{59}Fe and followed the labeled iron after injection into *HRG1*$^{+/+}$ and *HRG1*$^{-/-}$ mice. *HRG1*$^{+/+}$ donor mice were treated with phenylhydrazine to induce acute hemolytic anemia and stimulate erythropoiesis, followed by an injection of ^{59}Fe-citrate which is incorporated into heme of newly-formed RBCs. Three days later, ≈80% of ^{59}Fe label was incorporated into heme and the ^{59}Fe-labelled RBCs were opsonized and injected into *HRG1*$^{+/+}$ and *HRG1*$^{-/-}$ recipient mice (Franken et al., 2015; Soe-Lin et al., 2009) that had been maintained on a low-iron diet for six weeks (**Fig. 5A)**. The retention and distribution of ^{59}Fe in the tissues of the recipient mice were monitored over a period of 96 h. The spleens of *HRG1*$^{+/+}$ mice accumulated ^{59}Fe within 24 h followed by a decrease at 96 h with a concomitant increase of ^{59}Fe in the circulation and kidneys (**Fig. 5B)**. By contrast, the spleens of *HRG1*$^{-/-}$ mice accumulated more ^{59}Fe over the course of 96 h with limited amounts of ^{59}Fe in the circulation and kidneys, suggesting that the release of ^{59}Fe from phagocytosed RBCs was impaired (**Fig. 5B)**.

To discriminate ^{59}Fe from [^{59}Fe]heme, homogenized spleens were subjected to high-speed centrifugation to precipitate proteinase-resistant and detergent-insoluble fractions. The resulting supernatant was differentially extracted by ethyl-acetate to separate heme from iron. While *HRG1*$^{-/-}$ spleens accumulated significantly greater levels of ^{59}Fe compared to *HRG1*$^{+/+}$ spleens, these differences were primarily due to ^{59}Fe counts within the organic heme fraction ([^{59}Fe]heme) and not in the aqueous iron fraction (^{59}Fe) (**Fig. 5B, C)**.

A large portion of ^{59}Fe was detected in the detergent-insoluble fraction of *HRG1*$^{-/-}$ spleens (**Fig. 5C)** and livers (**Supplemental Fig. 5A)**. A proteinase and detergent resistant fraction enriched in iron is characteristic of hemozoin, a crystallized form of heme generated during the digestion of hemoglobin by blood-feeding parasites such as *Plasmodium* (Egan, 2008; Francis et al., 1997). To determine whether the insoluble fractions from *HRG1*$^{-/-}$ tissues had hemozoin-like properties, we treated the fractions with buffers known to dissolve hemozoin (**Fig. 5D)**. Spectroscopic analysis of the dissolved detergent-resistant fraction revealed absorption spectra characteristic of heme (**Fig. 5E, Supplemental Fig. 5B)**. High resolution X-ray powder diffraction of the purified insoluble fraction from the *HRG1*$^{-/-}$ spleens confirmed that the dark pigment is identical to malarial hemozoin (**Fig. 5F)** (Gildenhuys et al., 2013). The structure reveals a repeating unit of heme dimers linked together by iron-carboxylate bonds to one propionic acid side chain with the adjacent heme dimers forming stable chains by hydrogen bonding via the free propionate side chain (**Fig. 5G, Supplemental Fig. 5C)** (Coronado et al., 2014). Spectrophotometric analysis of the dissolved hemozoin fractions showed substantial amounts of hemozoin-heme present in the spleens and livers of *HRG1*$^{-/-}$ mice, but not in *HRG1*$^{+/+}$ mice (**Fig. 5H, Supplemental Fig. 5D)**. Notably, a significant amount of heme in non-hemozoin form was also found in *HRG1*$^{-/-}$ spleens (2-fold of *HRG1*$^{+/+}$; **Fig. 5H**).

Scanning electron microscopy images showed mammalian hemozoin was heterogeneous; purified hemozoin crystals from spleen and liver appeared larger than *Plasmodium* hemozoin, while bone marrow-purified hemozoin was similar in size (**Fig. 5I)**. Transmission electron microscopy with purified F4/80^{+} tissue-resident macrophages from the spleen and bone marrow showed that hemozoin was sequestered within a membrane-enclosed compartment (**Fig. 5J)**. However, isolated *HRG1*$^{-/-}$ monocytes that were differentiated into macrophages *in vitro* did not

contain any hemozoin (**Supplemental Fig. 5E)**, indicating that hemozoin formation occurs *in vivo* after tissue resident macrophages are established. Confocal microscopy using antibodies against LAMP1, which has been previously demonstrated to be a strong marker of erythrophagosomes in macrophages (Delaby et al., 2012; Huynh et al., 2007), showed that all of the hemozoin in isolated-F4/80^{+} macrophages from *HRG1*$^{-/-}$ bone marrow is enclosed within LAMP1-positive compartments (**Fig. 5K, Supplemental Fig. 5F)**. Furthermore, these hemozoin-containing LAMP1-positive vesicles were significantly larger (diameter 570 to 4300 nm) compared to typical lysosomes which range from 50 nm to 500 nm (Bandyopadhyay et al., 2014) (**Fig. 5K,** compare vesicles with white vs yellow arrows**; Supplemental Fig. 5G)**.

Intracellular hemozoin is typically known to be inert and ingested malarial hemozoin can remain unmodified for long periods of time within human monocytes (Schwarzer et al., 1993). To test whether mouse hemozoin could be used as a source of iron when macrophages are forced to undergo apoptosis, we administered clodronate liposomes to iron-deficient *HRG1*$^{+/+}$ and *HRG1*$^{-/-}$ mice. RES macrophages were completely depleted by day 3 post-injection but *HRG1*$^{-/-}$ spleens, livers and bone marrows still retained hemozoin, which were now extruded into the interstitial space (not shown). However, this hemozoin was not bioavailable as an iron source to correct iron deficiency anemia even after seven days (**Supplemental Fig. 5H)**. Altogether, these results strongly indicate that in the absence of *HRG1*, RES macrophages are unable to recycle and degrade heme from ingested RBC resulting in heme accumulation and biocrystallization into hemozoin within enlarged phagolysosomes.

HRG1 deficiency confers cellular heme tolerance during erythrophagocytosis

To evaluate the impact of HRG1 deficiency at the cellular level, we analyzed the ability of bone marrow-derived macrophages (BMDMs) to recycle heme-iron derived from

phagocytosed RBCs. Although *HRG1*$^{+/+}$ and *HRG1*$^{-/-}$ BMDMs engulfed similar numbers of opsonized RBCs (**Supplemental Fig. 6A**), HRG1-deficient cells accumulated significantly more heme even after 72 h post-EP (**Fig. 6A**). As heme is cytotoxic and damaging to macrophages (Kovtunovych et al., 2010), we measured cellular markers of oxidative stress during the two critical phases of heme-iron recycling after EP - the early (4 h) and late (24 h) phase. Reactive oxygen species (ROS) production (**Fig. 6B)** (Delaby et al., 2005; Kovtunovych et al., 2010) and the ratio of oxidized to reduced glutathione levels (GSSG:GSH) (**Fig. 6C)** was significantly lower in *HRG1*$^{-/-}$ cells during the early phase, when active digestion of red cells takes place. Consistent with this early suppression of ROS, lactate dehydrogenase (LDH) release into the growth medium (Rayamajhi et al., 2013) was also significantly reduced in *HRG1*$^{-/-}$ cells in the late phase (**Fig. 6D)**, with no loss in cell adherence (**Supplemental Fig. 6B)** (Delaby et al., 2005). Together, these results imply that HRG1 deficiency protects the macrophages from the damaging effects of EP (Delaby et al., 2005).

Haploinsufficiency of *HMOX1* in *HRG1*-deficient animals causes perinatal lethality

The *in vivo* and cell biological studies posit that loss of HRG1 confers heme tolerance by confining heme to the phagolysosome and preventing its degradation by HMOX1. However, EP studies reveal that HMOX1 induction and abundance were comparable between *HRG1*$^{+/+}$ and *HRG1*$^{-/-}$ BMDMs over 72 h post-EP (**Fig. 6E)** These results raised the possibility that, in the absence of HRG1, an alternate albeit less-efficient heme transport pathway could translocate heme from the phagolyosome for degradation by HMOX1. To evaluate the genetic contribution of HMOX1, we generated *HMOX1*$^{+/-}$*HRG1*$^{+/+}$ and *HMOX1*$^{+/-}$*HRG1*$^{-/-}$ double mutant mice. Analysis of offspring from *HMOX1*$^{+/-}$*HRG1*$^{+/+}$ and *HMOX1*$^{+/-}$*HRG1*$^{-/-}$ intercrosses showed reduced numbers of viable *HMOX1*$^{-/-}$ progeny (Observed/Expected: *HMOX1*$^{-/-}$*HRG1*$^{+/+}$ 9/64

versus *HMOX1*$^{-/-}$*HRG1*$^{-/-}$ 9/86) regardless of the presence of *HRG1* (**Fig. 6F, Supplemental Fig. 6C)**. Consistent with this observation, *HMOX1*$^{-/-}$*HRG1*$^{+/+}$ and *HMOX1*$^{-/-}$*HRG1*$^{-/-}$ mice showed similar reductions in RES macrophages and erythropoietic profiles from the bone marrow and spleen at ten weeks of age (**Supplemental Fig. 6D-I)**, and developed anemia as they grew older (not shown).

Unexpectedly, heterozygous offspring from *HMOX1*$^{+/-}$*HRG1*$^{-/-}$ intercrosses did not show Mendelian ratio at birth, with almost 40 % embryonic lethality (Observed/Expected: *HMOX1*$^{+/-}$ *HRG1*$^{+/+}$ 133/128 versus *HMOX1*$^{+/-}$*HRG1*$^{-/-}$ 108/172) (p<0.001 by chi-square test) (**Fig. 6F, Supplemental Fig. 6C)**. Flow cytometry analyses of *HMOX1*$^{+/-}$*HRG1*$^{-/-}$ mice showed an enhanced reduction in splenic RPMs (**Fig. 6G)** and total Ter-119^{+} cells in the bone marrow (**Fig. 6H)** compared to *HMOX1*$^{+/-}$*HRG1*$^{+/+}$ mice. The bone marrow subpopulations of Ter-119^{+} cells were also significantly reduced in populations II to V in *HMOX1*$^{+/-}$*HRG1*$^{-/-}$ mice (**Fig. 6I)**. The spleens of *HMOX1*$^{+/-}$*HRG1*$^{-/-}$ mice had fewer Ter-119^{+} cells with more immature Ter-119^{+} cells (**Fig. 6J, K)**, suggesting ineffective stress erythropoiesis. Together these results reveal that inhibition of HMOX1 in the absence of HRG1 has two different outcomes depending on the degree of HMOX1 impairment. Partial reduction or haploinsufficiency of *HMOX1*, as observed in *HMOX1*$^{+/-}$*HRG1*$^{-/-}$ mice, increases perinatal lethality and a shift to synthetic lethality. However, complete inhibition of *HMOX1* leads to loss in cell viability (**Supplemental Fig. 6J, K)** and greater embryonic mortality of *HMOX1*$^{-/-}$*HRG1*$^{-/-}$ and *HMOX1*$^{-/-}$*HRG1*$^{+/+}$ mice (**Supplemental Fig. 6C)**, demonstrating a delicate balance between heme transport and degradation.

DISCUSSION

Our results show that *HRG1*$^{-/-}$ mice are defective in transporting heme across the phagosomal membrane during EP, resulting in large amounts of heme accumulation and hemozoin formation within phagolysosomes of RES macrophages. Heme retention leads to impaired iron recycling for erythrocyte production in the bone marrow, stimulating extramedullary erythropoiesis similar to the effects caused by iron-deficiency (**Fig. 6L)**. However, the overall impact on RBC production and anemia is modest on a standard iron diet (380 ppm). These findings support the conclusion that mice on an iron-rich diet can circumvent a block in heme-iron recycling by relying more heavily on dietary iron for erythropoiesis (Ganz and Nemeth, 2006). This is in stark contrast to humans where the daily iron absorption does not exceed 10% of the amount of recycled iron utilized for erythropoiesis (Kautz and Nemeth, 2014; Muñoz et al., 2009; Winter et al., 2014). However, when *HRG1*$^{-/-}$ mice are fed a low-iron diet, the block in heme-iron recycling is exacerbated. Furthermore, when *HRG1*$^{-/-}$ mice encounter prolonged dietary iron limitation (8 to 20 weeks), they are unable to sustain erythropoiesis, implying that it takes approximately eight weeks for body iron stores to be depleted in the absence of heme-iron recycling. Indeed, results from the *in vivo* ^{59}Fe-labelled RBC studies show that the relative proportion of ^{59}Fe retained within the spleens of *HRG1*$^{-/-}$ mice are 50.3% hemozoin : 34.4% heme : 15.3% non-heme iron after 96 h (**Fig. 5C**). Assuming that ineffective heme-iron recycling reduces recycled iron according to the law of exponential decay (Leike, 2001) and RBCs have a lifespan of ~40 days, this ^{59}Fe distribution pattern would predict that *HRG1*$^{-/-}$ mice would become significantly anemic after six weeks as hemozoin accumulates after RBC turnover. We conclude that after six weeks on a low-iron diet, *HRG1*$^{-/-}$ mice reach a “metabolic

threshold" i.e. a physiological transition from an intermediate iron state to severe iron limitation, which eventually led to mortality in these animals (**Fig. 6L, right panel)**.

Even though *HRG1*$^{+/+}$ and *HRG1*$^{-/-}$ mice had similar hematocrits at five weeks on a low-iron diet, *HRG1*$^{-/-}$ mice were unable to undergo stress erythropoiesis and showed dysregulation of over 35 iron and heme metabolism genes in their spleens and livers. Typically under iron deficient conditions, the production of the liver hormone hepcidin is suppressed, which results in greater mobilization of iron by ferroportin to iron-deprived compartments (Ganz and Nemeth, 2006; Nemeth et al., 2004). The inability to sustain erythropoiesis, despite a significant suppression in hepatic hepcidin expression in *HRG1*$^{-/-}$ iron-deficient mice (**Supplemental Fig. 4G)**, suggest that these mice are iron-deprived even though the RES tissues are heme-iron loaded, i.e. systemic iron status is uncoupled from tissue and cellular iron status in the absence of *HRG1*. While hepatic hepcidin is considered to be the major facilitator of systemic iron homeostasis, recent studies have uncovered an autocrine role for locally-produced hepcidin in regulating cardiac iron homeostasis (Lakhal-Littleton et al., 2016). Indeed, *HRG1*$^{-/-}$ mice show elevated splenic hepcidin regardless of iron status (**Supplemental Fig. 4H)**, implying a role for splenic hepcidin in stress erythropoiesis.

In the absence of *HRG1*, heme accumulates in the erythrophagosome of RES macrophages in the form of hemozoin biocrystals. Heme-iron recycling of senescent erythrocytes occurs in the RES macrophages - mainly in the splenic RPMs and, to some extent, in liver Kupffer cells and bone marrow macrophages (Beaumont and Delaby, 2009; Ganz, 2012; Theurl et al., 2016). Our results establish a direct role for HRG1 in transporting heme from the phagolysosomal compartments to the cytosol for degradation by HMOX1. Unlike *HRG1*$^{-/-}$ mice, loss of *HMOX1* causes over 90% embryonic lethality. Why do *HRG1*$^{-/-}$ mice survive while

HMOX1$^{-/-}$ mice show high embryonic mortality? Our results show that in the absence of *HRG1*, high concentrations of heme is sequestered as hemozoin within the acidic phagolysosome, resulting in cellular heme tolerance. By contrast, in the absence of *HMOX1*, heme accumulates within the cytosol resulting in cytotoxicity and embryonic lethality. Genetic epistasis would have predicted that the heme sequestration would rescue the embryonic lethality of the *HMOX1*$^{-/-}$ *HRG1*$^{-/-}$ double knockout mice. Possible explanations for this unexpected finding could be that *HMOX1* has additional functions beyond heme degradation, or that the heme degradation products are required for cell differentiation and specification *in vivo*. Our results support both of these explanations and further reveal that *HRG1*$^{-/-}$ mice require a fully-operational heme degradation pathway to confer complete heme tolerance, as partial reduction of *HMOX1* in the absence of *HRG1* show significant embryonic lethality with severe impairment in macrophage and erythroblast maturation in the bone marrow and spleen (**Fig. 6F-K)**.

Blood-feeding parasites degrade hemoglobin in their digestive vacuole and accumulate heme in the form of hemozoin (Chen et al., 2001; Toh et al., 2010). Although the exact mechanisms of *in vivo* hemozoin formation are not well understood, it is generally agreed upon that hemozoin formation is a heme detoxification method used to protect the parasite from heme toxicity (Hempelmann, 2007; Toh et al., 2010). Hemozoin biocrystals are thought to be well-tolerated by both the parasite and subsequent host cells which ingest it, despite some reports on the inflammatory responses towards hemozoin ingestion (Basilico et al., 2003; Schwarzer et al., 1993). We found hemozoin within LAMP1-positive intracellular vesicles, which are typically between pH 4 and 6 (Johnson et al., 2016; Mellman et al., 1986). Acidic pH appears to be a common requirement for hemozoin formation in parasitic digestive vacuoles, *in vitro* and in macrophages (Egan et al., 2001; Shio et al., 2010). To our knowledge, hemozoin formation in

mammals has not been documented prior to this study. This phenomenon observed in *HRG1*$^{-/-}$ spleens, livers and bone marrows suggests that macrophages are able to elicit a protective mechanism against high concentrations of heme by exploiting the low pH environment of lysosomes. It is important to note that *HRG1*$^{-/-}$ mice have fewer RPMs, which implies that hemozoin sequestration may be incomplete or insufficient to confer complete heme tolerance, or that hemozoin itself could cause detrimental effects to these cells. Hemozoin in *HRG1*$^{-/-}$ RES macrophages leads to tissue heme accumulation in these mice without causing major damages to tissue architecture. We speculate that pharmacologic inhibition of HRG1 in humans would lead to tolerance and protection from heme toxicity and iron overload.

EXPERIMENTAL PROCEDURES

Animals

All mice used were housed in a 12 h light-dark cycle. For *HRG1* pups, genetic segregation was computed on 21-day old (P21) mice pups. *HRG1* mice were genotyped from tail genomic DNA extracts using a custom ordered TaqMan® SNP Genotyping Assays probe (ThermoFisher Scientific) on a Bio-rad CFX Connect system. For *HMOX1/HRG1* mice, genetic segregation was computed on 5-day old (P6) mice pups via toe-clip DNA extracts. *HMOX1* was genotyped by PCR using primers HMOX1 KO Forward 5'-GCTTGGGTGGAGAGGCTATTC-3', HMOX1 KO Reverse 5'-CAAGGTGAGATGACAGGAGATC-3', HMOX1 WT Forward 5'-GTACACTGACTGTGGGTGGGGGAG-3', HMOX1 WT Reverse 5'-AGGGCCGAGTAGATATGGTAC-3'. Mice in all studies were males unless otherwise noted, although initial experiments to exclude gender variation were done using both males and females. All animal protocols were approved by the Institutional Animal Care and Use Committee at the University of Maryland, College Park.

Generation of HRG1$^{-/-}$ mice

Guide and Cas9 RNAs: The guide RNA (5'-TAGGGACGGTGGTCTACCGACAACCGG-3') was purchased from Sage Laboratories 2033 Westport Center Drive, St Louis, MO. Cas 9 RNA was purchased from Trilink Biotechnologies, San Diego, CA. The guide RNA and Cas9 RNA were combined at a concentration of 5 ng/µl (each) in 10 mM Tris, 0.25 mM EDTA (pH 7.5) for injection.

Pronuclear Injection: Pronuclear injection was performed using standard procedures (Behringer et al., 2014). Briefly, fertilized eggs were collected from superovulated C57BL/6J x 129/SvJ F_1 females approximately 9 h after mating with C57BL/6J male mice. Pronuclei were injected with

a capillary needle with a 1-2 µm opening pulled with a Sutter P-1000 micropipette puller. The RNAs were injected using a FemtoJet 4i (Eppendorf) with continuous flow estimated to deposit approximately 2 pl of solution. Injected eggs were surgically transferred to pseudo-pregnant CB6 F_1 recipient females.

Genotyping: DNA was obtained from founder (F_0) animals by tail biopsy, amplified by PCR (Forward 5'-TGCACCTGTGACTCGGCG-3' Reverse 5'-TAGGTCCCGCCACGTTCATAA-3') and sequenced to determine the mutation. F_0 animals carrying mutations were crossed to C57BL/6 animals and the resulting heterozygous F_1 animals were either intercrossed to generate homozygous mutant animals or back crossed to C57BL/6 mice for propagation.

Dietary study

HRG1$^{+/+}$ and *HRG1*$^{-/-}$ mice obtained from *HRG1*$^{+/-}$ crosses were weaned at 21 days of age (P21) and placed on their respective diets, supplemented with deionized water. Standard rodent diet was obtained from Envigo and the 2 ppm (TD.09127) Fe diet was custom ordered from Envigo, Madison, WI. Body weights and feed intake per cage were measured weekly to ensure the conditions of the animals. Blood was collected by retro-orbital bleeding using microcapillary tubes (Fisher Scientific, cat. number 22-362566). At the end of five weeks, mice were sacrificed by cardiac perfusion using Dulbecco's phosphate-buffered saline (DPBS) (Gibco, cat. number 14190250) under anesthesia (10% ketamine, 8% xylazine mix). Prior to perfusion, whole blood was collected into tubes and allowed to clot at room temperature for 45 min and serum was separated from the sample by centrifugation at 2000 g for 10 min. For the prolonged dietary iron study where the Kaplan Meier survival curve was obtained, whole blood hematocrits were obtained every two weeks until week 14. All surviving *HRG1*$^{-/-}$ mice were sacrificed when the

survival rate fell below 50% (~week 16), while *HRG1*$^{+/+}$ mice were kept on the diets until week 18.

Immunohistochemistry and Histology

Paraffin-embedded tissue sections were processed for antigen retrieval by heat-induced epitope retrieval in citrate buffer pH 6 (DAKO, Glostrup, Denmark, cat. number S2367). After epitope retrieval, sections were then incubated with either rat anti-F4/80 (Invitrogen, cat. number MF48000) (1:1000 in blocking buffer TBS with 2% FBS) or rabbit anti-HRG1 (Zhang et al., 2018) (1:500) overnight at 4°C. Polyclonal HRG1 antibody serum was generated in rabbit using the C-terminal 17 amino acid peptide sequence (YAHRYRADFADIILSDF) of human HRG1 as antigen (Epitomics, Inc.). Sections were then incubated with secondary biotinylated anti-rat antibody (Vector labs, cat. number BA-9400) for 30 min at room temperature. Signals were detected by DAB substrate incubation and slides were lightly counterstained with hematoxylin. H&E and Perl's Prussian blue stainings were conducted by Histoserve, Inc.

Crude membrane prep and western blots for HRG1

Tissues were snap frozen in liquid nitrogen and ground using a ceramic pestle and mortar maintained ice-cold. In a dounce homogenizer, powdered tissue samples were added to membrane prep buffer (250 mM Sucrose, 1 mM EDTA, 10 mM Tris-HCl pH 7.4, 3X protease inhibitor cocktail). Samples were dounce homogenized until no obvious chunks of tissue were observed and the number of strokes used for homogenization was kept consistent across all samples. Homogenates were centrifuged at 800 g for 10 min at 4°C. The supernatant was transferred to ultracentrifugation tubes and spun at 100,000 g for 2 h at 4°C. The pellet from ultracentrifugation was then resuspended in lysis buffer (150 mM NaCl, 1 mM EDTA, 20 mM HEPES pH 7.4, 2% Triton-X, 3X protease inhibitor) and sonicated to ensure complete lysis. The

sample was then centrifuged at 11,000 g for 30 min at 4°C and the insoluble pelleted debris was discarded. Protein concentration of the supernatant was determined using the BCA assay (Pierce™ BCA Protein Assay Kit, ThermoFisher Scientific, cat. number 23225). Samples were mixed with SDS-loading buffer without heating and electrophoretically separated on a 4–20% Criterion™ TGX™ Precast Midi Protein Gel (Bio-rad, cat. number 5671094) and transferred to nitrocellulose membrane. Proteins were cross-linked to membranes by UV treatment and stained by ponceau S before incubation in blocking buffer (5% nonfat dry milk in 0.05% Tris-buffered saline-Tween 20, TBS-T) for 1 h at room temperature. Blots were then incubated overnight at 4 °C in blocking buffer containing rabbit anti-HRG1 antibody (1:300 dilution). After three washes in TBS-T, blots were incubated 1 h with horseradish peroxidase (HRP)-conjugated goat anti-rabbit IgG secondary antibody (1:20000; Invitrogen cat. Number 31460) in blocking buffer. Blots were then washed five times with TBS-T and signals were visualized by using enhanced chemiluminescence (SuperSignal West Pico, Pierce) and detected using ChemiDoc™ Imaging Systems (Bio-rad).

RNA Extraction and Quantitative Reverse-Transcriptase PCR Array

Total RNA was isolated from samples using TRIzol™ Reagent (ThermoFisher Scientific). cDNA synthesis was done using RT2 First Strand Kit (Qiagen). The Qiagen iron metabolism RT2 profiler array was custom built (Cat. number CLAM25204D) and used with RT2 SYBR Green Fluor qPCR mastermix (Qiagen) on a CFX Connect system (Bio-rad). Analysis of gene expression data was conducted using the online data analysis web portal provided by Qiagen. Briefly, Ct values for each gene in each group (eg. +/+, Standard diet) were obtained by taking the average across all mice (n=9 per group). ΔCt values were then obtained by the following formula: ΔCt = Ct (target gene) – Ct (housekeeping gene). The housekeeping gene used was

RPL13a. Gene expression was then calculated by the formula $2^{\wedge(-\Delta Ct)}$. *p* values for gene expression were calculated using ΔCt values, the corresponding standard deviations and n=9. The gene expression heatmap was generated by the Heatmapper software and clustering was performed using Pearson's distance measurement method with average clustering(Babicki et al., 2016).

Hemozoin extraction and quantification

Hemozoin extraction was performed according to the method of Deroost et al (Deroost et al., 2012). Approximately 50 to 100 mg perfused mouse liver or spleen were ground in liquid nitrogen with mortar and pestle. The ground powder was resuspended in five to ten volumes of homogenization buffer (50 mM Tris/ HCl pH 8.0, 5 mM $CaCl_2$, 50 mM NaCl, 1% Triton X-100 and 1% Proteinase K) and incubated overnight at 37°C with gentle shaking. For mice younger than three weeks, a whole liver or spleen was homogenized in minimum five volumes of homogenization buffer using FastPrep-24 (MP Bio) for 30 seconds at the 6.5 m/s setting, followed by overnight incubation at 37°C with gentle shaking. The proteinase K digested homogenate was then sonicated (Heat Systems-Ultrasonics, W350) for 1 min (20 W, pulse 1 sec) and centrifuged at 11,000 g for 45 min. The supernatant was collected in a new tube (Supernatant fraction) and the pellet was washed three times in washing buffer (100 mM $NaHCO_3$, pH 9.0 and 2% SDS) with 1 min sonication and 30 min centrifugation at 11,000 g. All the supernatant from three wash steps was collected and combined (Washing fraction). The remaining pellet (Pellet fraction, Hz) was dissolved and sonicated for 1 min in dissolving buffer (100 mM NaOH, 2% SDS and 3 mM EDTA) and centrifuged at 11,000 g for 30 min to discard any insolubles. For X-ray powder diffraction analysis, after the third wash, extracted Hz was washed five more times in distilled H_2O to remove the salts and detergents.

Heme concentrations of all three fractions (Supernatant, Washing and Pellet) were determined by the pyridine hemochromogen spectra method (Barr and Guo, 2015). A pyridine reagent mix was prepared by adding 3 mL 1 M NaOH and 6 mL pyridine to 19 mL H_2O in a glass container. For oxidized spectrum, 35 µL sample and 17 µL 15 mM $K_3Fe(CN)_6$ was mixed with 1 mL pyridine reagent in a cuvette and the spectrum at 400-675 nm was recorded (Shimadzu, UV-1601). Two to five mg of powdered $Na_2S_2O_4$ were added to the mixture and the reduced spectrum was recorded at 400-675 nm. Heme concentrations were calculated by subtracting the absorbance readings at 541, 556 and 575 nm in the oxidized spectrum from the corresponding readings in the reduced spectrum to get ΔA540, ΔA556 and ΔA575, using the extinction coefficients 20.7 / mM for ΔA540 ((ΔA556 - ΔA540) / 20.7) and 32.4 / mM for ΔA575 ((ΔA556-ΔA575) / 32.4), multiplying by the dilution factor of the sample (30.06 or (1000 + 35 + 17) / 35) and averaging the two results. Total heme (nmol / mg tissue) in each fraction was calculated by multiplying heme concentration with corresponding fraction volume, and then divided by the weight of homogenized tissue. Total heme (nmol / organ) in each fraction was calculated by multiplying total heme (nmol / mg tissue) with the total weight of corresponding organ. Total heme in the Supernatant and Washing fractions was summed up as non-Hz heme.

Inductively coupled plasma mass spectrometry (ICP-MS)

Prior to metal and heme analyses, frozen tissues were added to three volumes of pure water and homogenized in ceramic bead tubes (Qiagen) using an Omni Bead Ruptor 24. For metal analysis, homogenate aliquots were digested overnight in 5:1 HNO_3:H_2O_2, dried, and resuspended in 2% HNO_3 for analysis using an Agilent 7900 ICP-MS. Calibration standard solutions for determination of Fe, Zn, Cu & Mn were prepared from Agilent multi-element

calibration standard-2A. Protein concentrations of homogenates were determined by BCA Protein Assay (Thermo Fisher Scientific) for normalization.

Porphyrin extraction

Enough tissue homogenate preparation for ICP-MS was adjusted with water to make 50 µL of 5 mg/mL protein. The resulting suspension was extracted with 200 µL of EA (a mixture of four volumes of ethyl acetate to one volume glacial acetic acid), centrifuged at 13.5K rpm for 0.5 min, and the supernatant was removed. The residual was re-extracted with 200 µL of water-saturated EA and centrifuged similarly. The two supernatants were combined to make about 400 µL total volume, and 10 µL of which was injected into the UPLC. 20 µL of 2xNES (0.2M NaOH, 4% w/v SDS and 6 mM EDTA) added to the ~20µL residual. The resulting suspension was slowly mixed with 280 µL EA and then centrifuged at 13.5K rpm for 10 min. 10 µL of the supernatant was injected into the UPLC. In addition, 25 µL of un-extracted homogenate was mixed with 25 µL 2xNES, then with 350 µL EA, centrifuged at 13.5K rpm for 10 min and the supernatant was analyzed by UPLC.

UPLC

About 10 µL of sample extract was injected into a Waters Acquity UPLC system which included a binary solvent manager, sample manager, photodiode array detector (PDA), fluorescence detector (FLR), column heater and an Acquity UPLC BEH C18, 1.7 µM, 2.1 x 100 mm column. The PDA was set to measure hemin absorbance at 398 nm and the FLR to measure fluorescence of protoporphyrin IX (PPIX) at 404 nm excitation and 630 nm emission. Solvent A was 0.2% aqueous formic acid while Solvent B was 0.2% formic acid in methanol. The flow rate at 0.40 mL per min at 60˚C for the total run time of 7 min. The following successive gradient settings for run time in min versus A: 0.0, 80%; 2.5, 1%; 4.5, 1%; 5, 80%. The solvent composition

gradient settings were all linear. For standards, solutions of known concentrations of authentic hemin, PPIX dissolved in NES were extracted and then analyzed by UPLC as the samples.

Serum analyses

Serum iron, total iron binding capacity (TIBC) and transferrin saturation were measured using the Stanbio Iron & TIBC kit (VWR, cat. number 10152-550). Serum ferritin was quantified using the mouse ferritin ELISA kit (Abcam, cat. number ab157713). All kits were used according to the manufacturer's protocol.

^{59}Fe-labelled erythrocytes

$^{59}FeCl_3$ purchased from Perkin Elmer Life Sciences (cat. number NEZ037001MC) was mixed with sodium citrate (1:50 molar ratio in a total volume of 1 ml) and incubated for 1 h at room temperature to make ^{59}Fe-citrate. To generate ^{59}Fe-labelled red blood cells (RBCs), adult donor mice were first injected intraperitoneally once per day for 3 consecutive days with 50 mg/kg of phenylhydrazine (Sigma Aldrich, cat. number 114715) to induce anemia. Thirty min after the last phenylhydrazine dose, donor mice were injected intraperitoneally with 200 µl of radiolabeled ^{59}Fe-citrate (0.03 µM, ~12 million cpm). Following a 3-day rest, donor mice were anesthesized (10% Ketamine with 5% Xylazine) and whole blood was collected by retro-orbital bleeding using heparinized tubes. Whole blood was mixed with an equal volume of Alsever's solution (Sigma Aldrich, cat. number A3551). Mice were then sacrificed by cervical dislocation. ^{59}Fe-RBCs were collected by centrifugation and washed with DPBS before counting. ^{59}Fe-RBCs were opsonized with the mouse red blood cell antibody (Rockland, cat. number 210-4139); 20 µl of antibody was used for approximately 10^9 RBCs. The suspension was diluted to 10 ml with PBS, and incubated at 37°C on a rotating table for 20 min. The opsonized cells were washed twice with DPBS and counted again. The opsonized ^{59}Fe-RBCs were diluted with DPBS and

injected intraperitoneally into iron-deficient *HRG1*$^{+/+}$ and *HRG1*$^{-/-}$ mice (250 µl, 860,000 cpm per mouse). ^{59}Fe-RBCs -injected mice provided with food and water were sacrificed by CO_2 asphyxiation at 24 and 96 h post-injection. Whole blood was collected retro-orbitally for counting prior to sacrifice. Counts for separate tissues and spleen homogenates were collected on a Perkin Elmer (Packard) Wizard gamma counter (Efficiency ~21%) and whole carcass counts were collected using a Model 2200 scalar ratemeter (Efficiency ~0.3%) (LUDLUM measurements, Inc, Sweetwater, TX).

To count for ^{59}Fe in different extracts in spleens, spleens from the 96-h time-point were dounce homogenized in lysis buffer (1% Triton X-100, 1% proteinase K, Tris-HCl pH 8.0, NaCl, $CaCl_2$) and incubated overnight at 37°C. One-third of the homogenate was centrifuged at 11,000 g for 45 min to obtain the insoluble fraction. Ethyl acetate (EA) (1 part glacial acetic acid, 4 parts ethyl acetate) was added to the supernatant (1 part supernatant, 4 parts EA). The suspension was vortexed for 1 min and centrifuged at 800 g for 2 min to separate the organic and aqueous phase. This extraction was repeated once to the aqueous layer and EA extracts were pooled for counting.

Spleen and Bone marrow cells isolation

A mouse spleen was cut up into 1-3 mm pieces and placed in 5 ml of dissociation buffer (RPMI, 1X collagenase B, 1X DNase I) in tubes with a magnetic stir bar. Tubes were placed on a magnetic plate and spleens were dissociated at 37°C for 45 min. Homogenates were passed through 70 µm filters and cells were pelleted by centrifugation at 800 g for 10 min. Bone marrow cells were flushed from the femur and tibia of mice using a syringe and 18G needle with 10 ml of FACS buffer (DPBS with 2% FBS). Cell aggregates were dissociated by pipetting. Cell suspensions were centrifuged at 800 g for 5 min and supernatants were discarded. When red

blood cells (RBCs) were not needed for analysis, cells were resuspended in 1 ml of RBC lysis buffer (150 mM NH_4Cl, 10 mM $NaHCO_3$, 1.3 mM EDTA) and left at room temperature for 3 min. The lysis step was quenched by adding 5 ml of RPMI and cells were collected by centrifugation at 800 g for 10 min and resuspended in appropriate buffers for downstream application. From splenic and bone marrow cell suspensions, anti-F4/80 microbeads were used in conjunction with LS columns (Miltenyi Biotech, cat. number 130-110-443 and cat. number 130-042-401) according to the manufacturer's protocol. To isolate monocytes from bone marrow suspension, the mouse monocyte isolation kit was used (Miltenyi Biotech, cat. number 130-100-629). Monocytes and macrophages were cultured as described previously(White et al., 2013).

Preparation of opsonized RBCs/beads and EP

Whole blood was collected by retro-orbital bleeding using heparinized tubes from mice and mixed with an equal volume of Alsever's solution (Sigma Aldrich, cat. number A3551). RBCs were opsonized with the mouse red blood cell antibody (Rockland, cat. number 210-4139); 20 µl of antibody was used for approximately 10^9 RBCs.

For *in vitro* EP experiments, RBCs were added at a ratio of 1:10 (macrophage:RBCs) into cell culture media and applied to BMDMs. One h later, media was aspirated and cells were washed with DPBS and RBC lysis buffer (150 mM NH_4Cl, 10 mM $NaHCO_3$, 1.3 mM EDTA) before fresh media was replaced.

LDH assays

BMDMs were seeded in 6-well plates at a density of 4 x 10^6 cells per well and treated with the indicated treatments. Cells were harvested at indicated time points. LDH assays were conducted

using a kit purchased from Sigma (Cat. number TOX7) and assay was conducted according to the manufacturer's protocol.

ROS assays

BMDMs were seeded in 24-well plates at a density of 2 x 10^5 cells per well, treated with opsonized RBCs (1:10) and intracellular ROS was determined with a fluorometric intracellular ROS kit (Sigma-Aldrich, MAK142). Stained cells were visualized and captured using Leica DMI6000B with Cy5 filter set. The ImageJ software was applied to analyze regions of interest (ROIs) over multiple cells (n>50). The fluorescence intensity from all the ROIs was averaged, and the corresponding background average was subtracted to yield the signal intensity for each condition.

GSH quantification

BMDMs were seeded in 6-well plates at a density of 2 x 10^6 cells per well and treated with opsonized RBCs (1:10). Cells were harvested at indicated time points. LDH assays were conducted using a kit purchased from Abcam (Cat. number ab138881) and assay was conducted according to the manufacturer's protocol. The amount of GSH and GSSG were normalized to the protein concentration of each sample measured by a BCA protein assay.

Heme quantification and immunoblot of lysates

BMDMs were lysed in a lysis buffer (1% Trition X-100 and 2% SDS 62.5 mM NaCl, 1 mM EDTA, 20 mM Hepes pH 7.4, 2X protease inhibitor) and sonicated. Heme in the lysate was quantified by adding 5 µl lysate to 200 ul 2M oxalic acid and heated at 95°C for 30 minutes. A duplicate set of samples were kept at room temperature. Both sets were then measured for fluorescence at excitation and emission wavelengths of 400 nm and 662 nm, respectively. Values for the room temperature set were subtracted from that of the heated set and all measurements

were normalized to the protein concentration of the corresponding samples. Lysates were then subjected to SDS-PAGE and immunoblotting by HMOX1 antibody (Enzo, cat. number ADI-SPA-896, 1:1000 dilution) and HRG1 antibody as mentioned previously.

Immunofluorescence of LAMP1

Bone marrow isolated F4/80$^+$ macrophages (BMMs) were seeded onto coverslips and fixed with 4% PFA pH 7.4 for 40 min on ice, then washed twice with DPBS. Quenching was done using 0.1 M ethanolamine for 5 min and room temperature, twice. Coverslips were washed twice with DPBS and incubated in a buffer containing DPBS, 3% BSA, 0.4% saponin for 20 min at room temperature. Coverslips were then incubated in a buffer containing DPBS, 1% BSA and 0.15% saponin for 10 min before incubation with the LAMP1 primary antibody (Developmental Studies Hybridoma Bank, cat. number 1D4B, 1:100 dilution) for 1 h at room temperature. Cells were then washed three times with DPBS and incubated with the secondary antibody in the same buffer (Invitrogen, cat. number A-2121, 1:2000 dilution) for 1 h at room temperature. Coverslips were then washed three times with DPBS and stained with DAPI (1:30000 dilution) for 1 min before mounting with pro-long antifade (Thermofisher, cat. number P36930). Images were taken using the DeltaVision Elite Deconvolution microscope.

Flow cytometry

Prior to staining for flow cytometry, cells were resuspended in FACS buffer and counted to ensure that appropriate amounts of antibodies would be added. Cells were stained in 500 µl FACS buffer with the respective antibodies on ice for 30 min. After staining, cells were centrifuged at 800 g for 5 min and washed with FACS buffer before being resuspended in FACS buffer for analysis. For erythroid cell populations in the spleen and bone marrow, T cells, B cells, platelets, megakaryocytes and neutrophils were stained with fluorescein isothiocyanate

(FITC)-conjugated-CD4 (eBioscience, cat. number 14-0041-86), CD8a (eBioscience, cat. number 14-0081-86), B220 (eBioscience, cat. number 14-0452-86), CD41 (eBioscience, cat. number 14-0411-85), Gr-1 (eBioscience, cat. number 11-5931-82) and CD11b (eBioscience, cat. number 14-0112-86) and dump gating was used to exclude these cell populations during analysis. In addition, cells were stained with antibodies for allophycocyanin (APC)-conjugated Ter-119 (eBioscience, cat. number 47-5921-82) and eFluor-450-conjugated CD44 (eBioscience, cat. number 48-0441-82). For non-erythroid cell analysis, splenic cells were treated with RBC lysis buffer and stained with the following antibodies: phycoerythrin (PE)-conjugated Treml4 (Biolegend, San Diego, CA, cat. number 143304), APC-conjugated F4/80 (eBioscience, cat. number 17-4801-80), and PE-Cyanine7 (PE-Cy7)-conjugated CD11b (eBioscience, cat. number 25-0112-81). For all antibodies, 1 µl was used to stain 1 x 10^6 cells. Samples were run in a FACS Canto II or FACS Aria system (BD) and analysis was performed using FlowJo software (Tree Star Inc., Ashland, OR).

Gating of erythoid populations

The gating strategy for identifying different erythroid populations was as described elsewhere(Chen et al., 2009), using CD44 as a marker for different populations.

Transmission Electron Microscopy

Cells were seeded/cultured onto pre-cleaned Aclar disks as monolayers at a density of 1 x 10^6 cells per well. For fixation, the growing media was replaced with cold fixative solution (2.5% glutaraldehyde, 1% PFA; 0.1 M Cacodylate buffer, pH 7.2). The cells were incubated at 4°C overnight. The aclar disks were then gently rinsed twice with cacodylate buffer and post-fixed with 2% Osmium tetroxyde for 1 h at room temperature and pre-stained for 1 h with saturated filtered uranyl acetate at room temperature. Dehydration and infiltration followed by using

ethanol -graded series for 5 min each (50%; 70%; 95%-2X; 100%-3X) and pure acetone (3X 5 min). The aclar disks were infiltrated with 50% epon resin:acetone for 1 h, then with 75% epon resin for overnight and 100% epon resin over 8 h with 3 changes. Cells were embedded and polymerized at 60°C for 24 h. Ultrathin (70nm) sections were obtained with diamond knife (Diatome) and an ultratome Leica UC6 (Leica Microsystems, Vienna, Austria). Grids with sections were post stained with saturated uranyl acetate in dH2O for 20 min and with lead citrate for 10 min and imaged at 120 kV using JEOL-JEM 1400 Plus electron microscope (Tokyo, Japan).

Scanning Electron Microscopy

Hemozoin crystals were adhered to an aluminum stub with a carbon adhesive. The stubs were then coated in a sputter coater with a layer of gold/palladium to decrease charging of sample. Samples were examined using a F.E.I. Quanta 600 with field emission gun at 20KV and a working distance of approximately 10 nm.

X-ray powder diffraction analysis

The powder samples were mounted in a 0.4 mmϕ glass capillary. The X-ray powder diffraction data were measured using a large Debye-Scherrer camera with an imaging-plate as a detector installed at SPring-8 BL02B2 (Nishibori et al., 2001). The wavelength of incident X-ray was 0.800 Å. The exposure time was 17 min. The X-ray powder diffraction patterns were collected in 0.01° steps in 2θ. The data range of the present analysis was from 2.0° to 30.0° in 2θ, which corresponds to more than 1.55 Å in d-spacing range. Peak positions and relative intensities of powder profile were similar to those of β-hematin (Straasø et al., 2011). The rigid-body Rietveld analysis was carried out as an initial stage of refinement using the program SP (Nishibori et al.,

2007). The reliability factors of final Rietveld refinement were R_{wp}=2.6% and R_I=5.7%, respectively.

X-ray fluorescence microscopy (XFM)

Sample preparation was performed as described previously (Bhattacharjee et al., 2016). Briefly, macrophages were cultured directly onto sterilized silicon nitride membranes (1.5 x 1.5 mm, SiN, Silson Ltd, Northhampton, England) that had been incubated with sterile 0.01% Poly-L-lysine solution (Sigma-Aldrich, St Louis, MO). For the XFM experiments, the cells on the SiN membranes were fixed with 4% paraformaldehyde, rinsed sequentially with PBS, isotonic 100 mM ammonium acetate, DI water and air-dried.

XFM data were collected on the Bionanoprobe (Chen et al., 2015), beamline 9-ID-B, at the Advanced Photon Source, Argonne National Laboratory, Argonne, IL. The incident X-ray energy was tuned to 10 keV using a Si-monochromator, the monochromatic beam was focused to 80 x 80 nm using a Fresnel zone plate. The sample was placed at 15˚ to the incident X-ray beam and the resulting X-ray fluorescence was collected at 90º using an energy dispersive 4-element detector (Vortex ME-4, SII Nanotechnology, Northridge, CA). Elemental maps were generated by extracting, background subtracting, and fitting the fluorescence counts for each element at each point using the program MAPS (Vogt, 2003). The fluorescent photon counts were translated into µg/cm^2 using calibrated X-ray standards (AXO products, Dresden, Germany).

Statistical Analyses

All data are shown as means ± SEM unless otherwise stated. Means of groups were compared by using Student's unpaired t test. A p value of <0.05 was considered statistically significant. Analyses were performed using PRISM 7 software (GraphPad).

FIGURE LEGENDS

Figure 1. Reticuloendothelial tissues accumulate dark pigments in the absence of *HRG1*

A) Structure of the *SLC48A1* gene (which encodes HRG1) indicating the CRISPR target site in exon 1. **B)** Predicted topology of HRG1 protein; arrow indicates the site of the 2 basepair deletion resulting in frameshift mutation. **C)** Immunoblot analysis of membrane lysates prepared from spleens and livers of mice. Membranes were probed with anti-HRG1 antibody and then incubated with HRP-conjugated anti-rabbit secondary antibody. Each lane represents one animal. **D)** HRG1 immunohistochemistry analysis of paraffin-embedded tissue sections of mice. Tissue sections were probed with affinity-purified anti-HRG1 antibody and then incubated with HRP-conjugated anti-rabbit secondary antibody. Images shown are representative of at least 3 mice. **E-F)** Spleen wet weights and whole blood hematocrit from $HRG1^{+/+}$ and $HRG1^{-/-}$ mice. Each dot represents one mouse; mice were age (6 weeks) and sex-matched. **G)** Representative images of spleens, livers and bone marrows of age and sex-matched mice. *p<0.05.

Figure 2. $HRG1^{-/-}$ mice exhibit extramedullary erythropoiesis with fewer mature RPMs

Gating strategy of Ter-119^{+} cells in the (**A)** bone marrow and (**D)** spleen. Quantifications of total Ter-119^{+} cells in the (**B)** bone marrow and (**E)** spleen. The %single cells* on the y-axis denote single cells that are negative for CD4/8/41, B220 and Gr-1. **C)** Quantification of subpopulations of Ter-119^{+} cells represented as a percentage of total Ter-119^{+} cells in the bone marrow (n=7-12). **F)** Quantification of populations II and III of Ter-119^{+} cells represented as a percentage of total Ter-119^{+} cells in the spleen. Gating strategy (**G, I)** and quantification (**H, J)** of (**G, H)** splenic F4/80^{hi}Treml4^{+} red pulp macrophages (RPMs) and (**I, J)** F4/80^{hi} and F4/80^{lo}-CD11b^{hi} splenic monocytes. At least 100,000 single cells were analyzed per sample. Each dot represents one mouse. **p<0.05; **p<0.01.

Figure 3. Heme accumulates within RES macrophages of *HRG1*$^{-/-}$ mice

Histochemical staining of spleen, liver and bone marrow tissue sections of *HRG1*$^{+/+}$ and *HRG1*$^{-/-}$ mice with H&E (**A)** or Perl's Prussian blue (**B)**. Arrows indicate dark pigments in *HRG1*$^{-/-}$ tissues. Images shown are representative of at least 3 mice. Quantification of tissue iron (**C)** and heme (**D)** by ICP-MS and UPLC, respectively in tissues of mice fed a standard diet (n=6-17). **E)** F4/80 immunohistochemistry analysis of paraffin-embedded tissue sections of mice. Yellow arrows indicate dark pigments within F4/80-positive cells. At least 3 mice were analyzed per genotype. **F)** XFM of F4/80-positive bone marrow macrophages from *HRG1*$^{+/+}$ and *HRG1*$^{-/-}$ mice. **G)** Quantification of total cellular concentrations of indicated elements, organized by cellular abundance. **H)** ROI concentration within dark aggregates in *HRG1*$^{-/-}$ BMMs. Quantifications were measured for n=5 cells per genotype. *p<0.05; **p<0.01; ***p<0.001; ****p<0.0001**.**

Figure 4. Dietary iron deficiency disrupts iron metabolism gene expression in *HRG1*$^{-/-}$ mice and results in lethality

A) Kaplan-Meier survival curve of *HRG1*$^{+/+}$ and *HRG1*$^{-/-}$ mice placed on a low-iron (2ppm) diet (n=15-17, both males and females). **B-C)** Hematocrits of *HRG1*$^{+/+}$ and *HRG1*$^{-/-}$ mice placed on a standard or low-iron (2ppm) diet. Mice were placed on respective diets supplemented with deionized water starting at 21 days of age (week 0) (n=9-15 for 5-week data set; n=7-11 for 20-week data set). Quantification of tissue iron (**D)** and heme (**E)** by ICP-MS and UPLC respectively, in tissues of mice fed a low-iron (2ppm) diet (n=6-17). **F)** %Splenomegaly of *HRG1*$^{+/+}$ and *HRG1*$^{-/-}$ mice calculated by the percentage of increase in average wet weight of spleens between mice on low-iron versus standard iron diets (n=9-15); **G)** Ratio of 2ppm splenic Ter-119^{+} population II+III cells to that of standard diet mice (n=8-12); **H)** Quantification of total

Ter-119^{+} cells in the spleen. The %single cells* on the y-axis denote single cells that are negative for CD4/8/41, B220 and Gr-1. Each point represents one mouse. **I)** Quantification of subpopulations of Ter-119^{+} cells represented as a percentage of total Ter-119^{+} cells in the bone marrow (n=7-8); **J)** Quantifications of splenic RPMs in mice on a standard or low-iron (2ppm) diet, represented as a percentage of single cells analyzed (n=9-14). **K)** Quantification of the ratio of F4/80^{hi} to F4/80^{lo}CD11b^{hi} splenic monocytes from mice on a standard or low-iron (2ppm) diet (n= 9-15). At least 100,000 single cells were analyzed per sample. **L)** Gene expression heat map of 90 iron metabolism genes in spleens from mice on standard or low-iron (2ppm) diet. Pearson correlation was used for comparison; average linkage (n=9 per group, per genotype). *p<0.05; **p<0.01; ***p<0.001; ****p<0.0001.

Figure 5. Loss of *HRG1* produces hemozoin biocrystals within enlarged lysosomes due to impaired erythrophagocytosis

A) Experimental design of ^{59}Fe labeling and *in vivo* recycling. **B)** Quantification of ^{59}Fe retained in tissues, represented as the ratio of the amount of radioactivity within an organ to that of the entire animal. **C)** ^{59}Fe retained in differentially extracted fractions of the spleen at 96 h, represented as counts per min. Total homogenate: homogenized and proteinase-treated whole spleen; Organic: ethyl acetate extractable [^{59}Fe]heme; Aqueous: ethyl acetate non-extractable ^{59}Fe; Insoluble fraction: proteinase-insoluble fraction containing ^{59}Fe (n=4-6 across all groups and timepoints). **D)** Image of insoluble fractions before and after dissolving in buffer. **E)** Visible spectra of dissolved insoluble fractions. **F)** Powder x-ray diffraction of purified insoluble fraction from *HRG1*$^{-/-}$ spleens (red: measured data; dark blue: calculated pattern; light blue: background; green: structural plot) **G)** Chemical structure of hemozoin from *HRG1*$^{-/-}$ mice. **H)** Quantification of spenic heme by spectrophotometric measurements (n=3). **I)** Scanning electron microscopy of

hemozoin isolated from *Plasmodium*, *HRG1*$^{-/-}$ spleen, liver, and bone marrow. **J)** Transmission electron microscopy of F4/80^{+} bone marrow and splenic macrophages from *HRG1*$^{+/+}$ and *HRG1*$^{-/-}$ mice. At least 3 cells were imaged per genotype. **K)** Confocal microscopy of bone marrow macrophages from *HRG1*$^{+/+}$ and *HRG1*$^{-/-}$ mice probed with anti-LAMP1 antibody and secondary alexa-488 antibody. Hemozoin is pseudocolored as orange. White arrow points to hemozoin-laden vesicle, yellow arrow points to non hemozoin-laden vesicle. At least 20 cells were analyzed per genotype. *p<0.05; **p<0.01.

Figure 6. *HRG1* deficiency confers cellular heme tolerance during erythrophagocytosis and haploinsufficiency of *HMOX1* in *HRG1*-deficient animals causes perinatal lethality

A) Images of cell lysates and quantification of heme content in *HRG1*$^{+/+}$ and *HRG1*$^{-/-}$ BMDMs at basal (no treatment), 24 h, 48 h and 72 h post-EP (erythrophagocytosis). Results are representative of at least two experiments. **B)** Quantification of intracellular reactive oxygen species (ROS) in *HRG1*$^{+/+}$ and *HRG1*$^{-/-}$ BMDMs at basal, 4 h and 24 h post-EP. **C)** Ratio of cellular GSSG:GSH in *HRG1*$^{+/+}$ and *HRG1*$^{-/-}$ BMDMs at basal, 4 h and 24 h post-EP. Values for 4 h and 24 h are normalized to basal values. The values shown are a combination of two representative biological replicates. **D)** LDH content in cells and media of *HRG1*$^{+/+}$ and *HRG1*$^{-/-}$ BMDMs at 4 h and 24 h post-EP, represented as percentage of total LDH in cells and media. **E)** Immunoblots of HMOX1 and HRG1 protein of BMDM lysates shown in (A). **F)** Percentages of pups born of the indicated genotypes for *HMOX1*$^{+/-}$ intercrosses, either on a *HRG1*$^{+/+}$ or *HRG1*$^{-/-}$ background. **G)** Quantification of splenic RPMs in *HMOX1*$^{+/-}$*HRG1*$^{+/+}$ and *HMOX1*$^{+/-}$*HRG1*$^{-/-}$ mice by flow cytometry. **H)** Quantification of total Ter-119^{+} cells in the bone marrow. The %single cells* on the y-axis denote single cells that are negative for CD4/8/41, B220 and Gr-1. **I)** Quantification of subpopulations of Ter-119^{+} cells represented as a percentage of total Ter-

119^+ cells in the bone marrow. **J)** Quantification of total Ter-119^+ cells in the spleen. The %single cells* on the y-axis denote single cells that are negative for CD4/8/41, B220 and Gr-1. **K)** Quantification of populations II and III of Ter-119^+ cells represented as a percentage of total Ter-119^+ cells in the spleen. At least 100,000 single cells were analyzed per sample. Each dot represents one mouse. Both male and female mice were analyzed in the experiments conducted in Figure 6. **L)** Proposed model for the *in vivo* and *in vitro* function of *HRG1* in heme-iron recycling of RBCs under systemic iron replete and deficient conditions. *p<0.05; **p<0.01; ****p<0.0001**.**

Supplemental figure 1

A) Chromatogram of genomic DNA sequencing from mice indicating 2 basepair deletion. **B)** Mendelian distribution of P21 pups derived from *HRG1*$^{+/-}$ intercrosses.

Supplemental figure 2

A) Gating of bone marrow Ter-119^+ subpopulations. **B)** Gating of splenic Ter-119^+ population II+III. **C-D)** Gating of splenic RPMs and monocytes. Individual plots shown are representative of all mice analyzed per group.

Supplemental Figure 3

A-E) Quantification of tissue iron (Fe), copper (Cu), zinc (Zn), manganese (Mn) and heme (n=6-17). Heme was undetectable in brain tissue. F4/80 immunohistochemistry of spleen (**F)**, liver (**G)** and bone marrow (**H)** sections. *p<0.05; **p<0.01; ***p<0.001; ****p<0.0001**.**

Supplemental Figure 4

A) Quantification of tissue iron (Fe) (n=6-17). **B)** Quantification of total Ter-119^+ cells represented as a percentage of all single cells analyzed in the bone marrow. The %single cells*

on the y-axis denote single cells that are negative for CD4/8/41, B220 and Gr-1. At least 100,000 single cells were analyzed per sample. Gating of **C)** splenic Ter-119^{+} populations II+III and **D)** bone marrow Ter-119^{+} subpopulations. **E, F)** Gating of splenic RPMs and monocytes. Individual plots shown are representative of all mice analyzed per group. **G)** Gene expression heat map of 90 iron metabolism genes in livers from mice on standard or low iron (2 ppm) diet. Pearson correlation was used for comparison; average linkage (n=9 per group, per genotype). Gene expression by qPCR of iron metabolism genes in spleens (**H, top and bottom panel separated by expression level)** and livers (**I)** of *HRG1*$^{+/+}$ and *HRG1*$^{-/-}$ mice on indicated diets (n=9 mice per group). Gene expression was calculated as described in the experimental procedures section. **p*<0.05; ***p*<0.01; ****p*<0.001; *****p*<0.0001**.**

Supplemental Figure 5

A) ^{59}Fe retained in differentially extracted fractions of the liver at 96 h, represented as counts per min. Total homogenate: homogenized and proteinase-treated whole spleen; Organic: ethyl acetate extractable [^{59}Fe]heme; Aqueous: ethyl acetate non-extractable ^{59}Fe; Insoluble fraction: proteinase-insoluble fraction containing ^{59}Fe. n=4-6. **B)** Images of different fractions of spleen homogenates, accompanied by spectrophotometric measurements of each fraction (lower panel). **C)** Chemical structure (rotated view) of hemozoin from *HRG1*$^{-/-}$ mice. **D)** Quantification of liver heme by spectrophotometric measurements (n=3). **E)** TEM of *in vitro*-differentiated bone marrow macrophages and isolated bone marrow monocytes. At least 3 cells were imaged per genotype. **F)** LAMP1 immunofluorescence on F4/80^{+} bone marrow macrophages from *HRG1*$^{+/+}$ and *HRG1*$^{-/-}$ mice. **G)** Diameter of LAMP1-positive vesicles observed in F4/80^{+} bone marrow macrophages. In both *HRG1*$^{+/+}$ and *HRG1*$^{-/-}$ cells, the diameters of LAMP1-positive structures with distinguishable boundaries were quantified manually by ImageJ software analysis.

HRG1$^{+/+}$: 4 cells, 3-5 structures per cell; *HRG1*$^{-/-}$: 11 cells, 3-12 structures per cell. (**H)** Hematocrits of iron-deficient *HRG1*$^{+/+}$ and *HRG1*$^{-/-}$ mice treated with control or clodronate liposomes (n=6-14). *p<0.05, ***p<0.001.

Supplemental Figure 6

(A) Representative images of *HRG1*$^{+/+}$ and *HRG1*$^{-/-}$ BMDMs post-EP. **B) R**epresentative images of intracellular reactive oxygen species (ROS) in *HRG1*$^{+/+}$ and *HRG1*$^{-/-}$ BMDMs at the indicated timepoints post-treatments. **C)** Observed and expected numbers of pups born of the indicated genotypes for *HMOX1*$^{+/-}$ intercrosses, either on a *HRG1*$^{+/+}$ or *HRG1*$^{-/-}$ background. Quantification of splenic RPMs (**D)** and bone marrow macrophages (BMMs) (**E)** in *HMOX1*$^{-/-}$ *HRG1*$^{+/+}$ and *HMOX1*$^{-/-}$*HRG1*$^{-/-}$ mice by flow cytometry. **F)** Quantification of total Ter-119^{+} cells in the bone marrows of *HMOX1*$^{-/-}$*HRG1*$^{+/+}$ and *HMOX1*$^{-/-}$*HRG1*$^{-/-}$ mice. **G)** Quantification of subpopulations of Ter-119^{+} cells represented as a percentage of total Ter-119^{+} cells in the bone marrow. **H)** Quantification of total Ter-119^{+} cells in the spleen. The %single cells* on the y-axis denote single cells that are negative for CD4/8/41, B220 and Gr-1. **I)** Quantification of populations II and III of Ter-119^{+} cells represented as a percentage of total Ter-119^{+} cells in the spleen. At least 100,000 single cells were analyzed per sample. Each dot represents one mouse. **J)** LDH content in cells and media of *HMOX1*$^{-/-}$*HRG1*$^{+/+}$ and *HMOX1*$^{-/-}$*HRG1*$^{-/-}$ BMDMs post-erythrophagocytosis (EP), represented as percentage of total LDH in cells and media. **K)** Representative images of *HMOX1*$^{-/-}$*HRG1*$^{+/+}$ and *HMOX1*$^{-/-}$*HRG1*$^{-/-}$ BMDMs post-EP.

Supplemental information.

Supplemental Information includes 6 figures and 3 tables.

ACKNOWLEDGEMENTS.

We thank Hector Bergonia for help with the heme/UPLC measurements; Stacie Anderson and Martha Kirby for assistance with flow cytometry analyses; Edward Case for ^{59}Fe calibration and counting; Hidetaka Kasai and Shogo Kawaguchi for x-ray powder diffraction data collection; Paul Sigala for providing *Plasmodium* hemozoin; Si Chen at the Advanced Photon Source for assistance with the XFM experiments; and Susumu Tonegawa and Tracey Rouault for the *HMOX1* mice. This work was supported by funding from the National Institutes of Health DK85035 and ES025661 (IH); the Utah Center for Iron and Heme Disorders was supported by funding from DK110858 (JP); and the Intramural Program of the National Human Genome Research Institute (LJG, DB). We acknowledge use of the Advanced Photon Source at Argonne National Laboratory, supported by the Department of Energy, Office of Science, Office of Basic Energy Sciences, under contract no. DE-AC02-06CH11357. The synchrotron experiments were performed at SPring-8 BL02B2 with the approval of the Japan Synchrotron Radiation Research Institute (JASRI) as a Partner User (Proposal No. 2017A0074). The funders had no role in study design, data collection and analysis, decision to publish, or preparation of the manuscript.

AUTHOR CONTRIBUTIONS.

Experimental design and execution were as follows: Mouse, cell biology and biochemical experiments R.P., X.Y., N.R., J.Z., A.R., L.J.G., W.R.S., J.J., D.B., I.H.; X-ray powder diffraction E.N. and H.S.; macrophage experiments and data analyses M.Z.A. and M.H.; X-ray fluorescence microscopy M.R.; heme and iron measurements L.K.J. and J.P.; R.P. and I.H. wrote the manuscript. All authors discussed the results and commented on the manuscript.

AUTHOR INFORMATION.

IH is the President and Founder of Rakta Therapeutics Inc. (College Park, MD), a company involved in the development of heme transporter-related diagnostics. He declares no other competing financial interests.

REFERENCES

Babicki, S., Arndt, D., Marcu, A., Liang, Y., Grant, J.R., Maciejewski, A., and Wishart, D.S. (2016). Heatmapper: web-enabled heat mapping for all. Nucleic acids research *44*, W147-153.

Bandyopadhyay, D., Cyphersmith, A., Zapata, J.A., Kim, Y.J., and Payne, C.K. (2014). Lysosome transport as a function of lysosome diameter. PLoS One *9*, e86847.

Barr, I., and Guo, F. (2015). Pyridine Hemochromagen Assay for Determining the Concentration of Heme in Purified Protein Solutions. Bio Protoc *5*.

Basilico, N., Tognazioli, C., Picot, S., Ravagnani, F., and Taramelli, D. (2003). Synergistic and antagonistic interactions between haemozoin and bacterial endotoxin on human and mouse macrophages. Parassitologia *45*, 135-140.

Beaumont, C., and Delaby, C. (2009). Recycling iron in normal and pathological states. Semin Hematol *46*, 328-338.

Behringer, M., Gruetzner, S., McCourt, M., and Mester, J. (2014). Effects of weight-bearing activities on bone mineral content and density in children and adolescents: a meta-analysis. Journal of bone and mineral research : the official journal of the American Society for Bone and Mineral Research *29*, 467-478.

Bhattacharjee, A., Yang, H., Duffy, M., Robinson, E., Conrad-Antoville, A., Lu, Y.W., Capps, T., Braiterman, L., Wolfgang, M., Murphy, M.P., *et al.* (2016). The Activity of Menkes Disease Protein ATP7A Is Essential for Redox Balance in Mitochondria. The Journal of biological chemistry *291*, 16644-16658.

Chen, K., Liu, J., Heck, S., Chasis, J.A., An, X., and Mohandas, N. (2009). Resolving the distinct stages in erythroid differentiation based on dynamic changes in membrane protein expression during erythropoiesis. Proc Natl Acad Sci U S A *106*, 17413-17418.

Chen, M.M., Shi, L., and Sullivan, D.J., Jr. (2001). Haemoproteus and Schistosoma synthesize heme polymers similar to Plasmodium hemozoin and beta-hematin. Molecular and biochemical parasitology *113*, 1-8.

Chen, S., Paunesku, T., Yuan, Y., Jin, Q., Hornberger, B., Flachenecker, C., Lai, B., Brister, K., Jacobsen, C., Woloschak, G., *et al.* (2015). The Bionanoprobe: Synchrotron-based Hard X-ray Fluorescence Microscopy for 2D/3D Trace Element Mapping. Micros Today *23*, 26-29.

Coronado, L.M., Nadovich, C.T., and Spadafora, C. (2014). Malarial Hemozoin: From target to tool. Biochimica et biophysica acta *1840*, 2032-2041.

Delaby, C., Pilard, N., Hetet, G., Driss, F., Grandchamp, B., Beaumont, C., and Canonne-Hergaux, F. (2005). A physiological model to study iron recycling in macrophages. Exp Cell Res *310*, 43-53.

Delaby, C., Rondeau, C., Pouzet, C., Willemetz, A., Pilard, N., Desjardins, M., and Canonne-Hergaux, F. (2012). Subcellular localization of iron and heme metabolism related proteins at early stages of erythrophagocytosis. PLoS One *7*, e42199.

Deroost, K., Lays, N., Noppen, S., Martens, E., Opdenakker, G., and Van den Steen, P.E. (2012). Improved methods for haemozoin quantification in tissues yield organ-and parasite-specific information in malaria-infected mice. Malar J *11*, 166.

Dutra, F.F., Alves, L.S., Rodrigues, D., Fernandez, P.L., de Oliveira, R.B., Golenbock, D.T., Zamboni, D.S., and Bozza, M.T. (2014). Hemolysis-induced lethality involves inflammasome activation by heme. Proc Natl Acad Sci U S A *111*, E4110-4118.

Egan, T.J. (2008). Haemozoin formation. Molecular and biochemical parasitology *157*, 127-136.

Egan, T.J., Mavuso, W.W., and Ncokazi, K.K. (2001). The mechanism of beta-hematin formation in acetate solution. Parallels between hemozoin formation and biomineralization processes. Biochemistry *40*, 204-213.

Fibach, E., and Rachmilewitz, E. (2008). The role of oxidative stress in hemolytic anemia. Curr Mol Med *8*, 609-619.

Francis, S.E., Sullivan, D.J., Jr., and Goldberg, D.E. (1997). Hemoglobin metabolism in the malaria parasite Plasmodium falciparum. Annual review of microbiology *51*, 97-123.

Franken, L., Klein, M., Spasova, M., Elsukova, A., Wiedwald, U., Welz, M., Knolle, P., Farle, M., Limmer, A., and Kurts, C. (2015). Splenic red pulp macrophages are intrinsically superparamagnetic and contaminate magnetic cell isolates. Scientific Reports *5*.

Ganz, T. (2012). Macrophages and systemic iron homeostasis. J Innate Immun *4*, 446-453.

Ganz, T., and Nemeth, E. (2006). Regulation of iron acquisition and iron distribution in mammals. Biochimica et biophysica acta *1763*, 690-699.

Ganz, T., and Nemeth, E. (2012). Hepcidin and iron homeostasis. Biochimica et biophysica acta *1823*, 1434-1443.

Garratty, G. (2009). Drug-induced immune hemolytic anemia. Hematology Am Soc Hematol Educ Program, 73-79.

Gildenhuys, J., le Roex, T., Egan, T.J., and de Villiers, K.A. (2013). The single crystal X-ray structure of β-hematin DMSO solvate grown in the presence of chloroquine, a β-hematin growth-rate inhibitor. Journal of the American Chemical Society *135*, 1037-1047.

Haldar, M., Kohyama, M., So, A.Y., Kc, W., Wu, X., Briseno, C.G., Satpathy, A.T., Kretzer, N.M., Arase, H., Rajasekaran, N.S., *et al.* (2014). Heme-mediated SPI-C induction promotes monocyte differentiation into iron-recycling macrophages. Cell *156*, 1223-1234.

Hempelmann, E. (2007). Hemozoin biocrystallization in Plasmodium falciparum and the antimalarial activity of crystallization inhibitors. Parasitology research *100*, 671-676.

Huynh, K.K., Eskelinen, E.L., Scott, C.C., Malevanets, A., Saftig, P., and Grinstein, S. (2007). LAMP proteins are required for fusion of lysosomes with phagosomes. EMBO J *26*, 313-324.

Johnson, D.E., Ostrowski, P., Jaumouillé, V., and Grinstein, S. (2016). The position of lysosomes within the cell determines their luminal pH. The Journal of Cell Biology *212*, 677-692.

Kautz, L., and Nemeth, E. (2014). Molecular liaisons between erythropoiesis and iron metabolism. Blood *124*, 479-482.

Keel, S.B., Doty, R.T., Yang, Z., Quigley, J.G., Chen, J., Knoblaugh, S., Kingsley, P.D., De Domenico, I., Vaughn, M.B., Kaplan, J., *et al.* (2008). A heme export protein is required for red blood cell differentiation and iron homeostasis. Science *319*, 825-828.

Klei, T.R.L., Meinderts, S.M., van den Berg, T.K., and van Bruggen, R. (2017). From the Cradle to the Grave: The Role of Macrophages in Erythropoiesis and Erythrophagocytosis. Frontiers in Immunology *8*.

Knutson, M.D., Oukka, M., Koss, L.M., Aydemir, F., and Wessling-Resnick, M. (2005). Iron release from macrophages after erythrophagocytosis is up-regulated by ferroportin 1 overexpression and down-regulated by hepcidin. Proceedings of the National Academy of Sciences of the United States of America *102*, 1324-1328.

Knutson, M.D., Vafa, M.R., Haile, D.J., and Wessling-Resnick, M. (2003). Iron loading and erythrophagocytosis increase ferroportin 1 (FPN1) expression in J774 macrophages. Blood *102*, 4191-4197.

Kovtunovych, G., Eckhaus, M.A., Ghosh, M.C., Ollivierre-Wilson, H., and Rouault, T.A. (2010). Dysfunction of the heme recycling system in heme oxygenase 1-deficient mice: effects on macrophage viability and tissue iron distribution. Blood *116*, 6054-6062.

Kovtunovych, G., Ghosh, M.C., Ollivierre, W., Weitzel, R.P., Eckhaus, M.A., Tisdale, J.F., Yachie, A., and Rouault, T.A. (2014). Wild-type macrophages reverse disease in heme oxygenase 1-deficient mice. Blood *124*, 1522-1530.

Lakhal-Littleton, S., Wolna, M., Chung, Y.J., Christian, H.C., Heather, L.C., Brescia, M., Ball, V., Diaz, R., Santos, A., Biggs, D., *et al.* (2016). An essential cell-autonomous role for hepcidin in cardiac iron homeostasis. Elife *5*.

Larsen, R., Gouveia, Z., Soares, M.P., and Gozzelino, R. (2012). Heme cytotoxicity and the pathogenesis of immune-mediated inflammatory diseases. Front Pharmacol *3*, 77.

Leike, A. (2001). Demonstration of the exponential decay law using beer froth. European Journal of Physics *23*, 21-26.

Lenox, L.E., Perry, J.M., and Paulson, R.F. (2005). BMP4 and Madh5 regulate the erythroid response to acute anemia. Blood *105*, 2741-2748.

Mazzaccara, C., Labruna, G., Cito, G., Scarfo, M., De Felice, M., Pastore, L., and Sacchetti, L. (2008). Age-Related Reference Intervals of the Main Biochemical and Hematological Parameters in C57BL/6J, 129SV/EV and C3H/HeJ Mouse Strains. PLoS One *3*, e3772.

Mellman, I., Fuchs, R., and Helenius, A. (1986). Acidification of the endocytic and exocytic pathways. Annual review of biochemistry *55*, 663-700.

Muñoz, M., Villar, I., and García-Erce, J.A. (2009). An update on iron physiology. World journal of gastroenterology *15*, 4617-4626.

Nemeth, E., Tuttle, M.S., Powelson, J., Vaughn, M.B., Donovan, A., Ward, D.M., Ganz, T., and Kaplan, J. (2004). Hepcidin Regulates Cellular Iron Efflux by Binding to Ferroportin and Inducing Its Internalization. Science *306*, 2090-2093.

Nishibori, E., Sunaoshi, E., Yoshida, A., Aoyagi, S., Kato, K., Takata, M., and Sakata, M. (2007). Accurate structure factors and experimental charge densities from synchrotron X-ray powder diffraction data at SPring-8. Acta Crystallographica Section A *63*, 43-52.

Nishibori, E., Takata, M., Kato, K., Sakata, M., Kubota, Y., Aoyagi, S., Kuroiwa, Y., Yamakata, M., and Ikeda, N. (2001). The large Debye–Scherrer camera installed at SPring-8 BL02B2 for charge density studies. Journal of Physics and Chemistry of Solids *62*, 2095-2098.

Orf, K., and Cunnington, A.J. (2015). Infection-related hemolysis and susceptibility to Gram-negative bacterial co-infection. Front Microbiol *6*, 666.

Perry, J.M., Harandi, O.F., Porayette, P., Hegde, S., Kannan, A.K., and Paulson, R.F. (2009). Maintenance of the BMP4-dependent stress erythropoiesis pathway in the murine spleen requires hedgehog signaling. Blood *113*, 911-918.

Poss, K.D., and Tonegawa, S. (1997a). Heme oxygenase 1 is required for mammalian iron reutilization. Proc Natl Acad Sci U S A *94*, 10919-10924.

Poss, K.D., and Tonegawa, S. (1997b). Reduced stress defense in heme oxygenase 1-deficient cells. Proc Natl Acad Sci U S A *94*, 10925-10930.

Raja, K.B., Pountney, D.J., Simpson, R.J., and Peters, T.J. (1999). Importance of anemia and transferrin levels in the regulation of intestinal iron absorption in hypotransferrinemic mice. Blood *94*, 3185-3192.

Rayamajhi, M., Zhang, Y., and Miao, E.A. (2013). Detection of pyroptosis by measuring released lactate dehydrogenase activity. Methods Mol Biol *1040*, 85-90.

Schwarzer, E., Turrini, F., Giribaldi, G., Cappadoro, M., and Arese, P. (1993). Phagocytosis of P. falciparum malarial pigment hemozoin by human monocytes inactivates monocyte protein kinase C. Biochimica et biophysica acta *1181*, 51-54.

Seixas, E., Gozzelino, R., Chora, A., Ferreira, A., Silva, G., Larsen, R., Rebelo, S., Penido, C., Smith, N.R., Coutinho, A., *et al.* (2009). Heme oxygenase-1 affords protection against noncerebral forms of severe malaria. Proc Natl Acad Sci U S A *106*, 15837-15842.

Shio, M.T., Kassa, F.A., Bellemare, M.J., and Olivier, M. (2010). Innate inflammatory response to the malarial pigment hemozoin. Microbes and infection *12*, 889-899.

Sinclair, P.R., Gorman, N., and Jacobs, J.M. (2001). Measurement of heme concentration. Curr Protoc Toxicol *Chapter 8*, Unit 8.3.

Socolovsky, M. (2007). Molecular insights into stress erythropoiesis. Current opinion in hematology *14*, 215-224.

Soe-Lin, S., Apte, S.S., Andriopoulos, B., Jr., Andrews, M.C., Schranzhofer, M., Kahawita, T., Garcia-Santos, D., and Ponka, P. (2009). Nramp1 promotes efficient macrophage recycling of iron following erythrophagocytosis in vivo. Proc Natl Acad Sci U S A *106*, 5960-5965.

Sorbie, J., and Valberg, L.S. (1974). Iron balance in the mouse. Laboratory animal science *24*, 900-904.

Straasø, T., Kapishnikov, S., Kato, K., Takata, M., Als-Nielsen, J., and Leiserowitz, L. (2011). The Role of the Four Stereoisomers of the Heme Fe–O Cyclic Dimer in the Crystalline Phase Behavior of Synthetic Hemozoin: Relevance to Native Hemozoin Crystallization. Crystal Growth & Design *11*, 3342-3350.

Theurl, I., Hilgendorf, I., Nairz, M., Tymoszuk, P., Haschka, D., Asshoff, M., He, S., Gerhardt, L.M., Holderried, T.A., Seifert, M., *et al.* (2016). On-demand erythrocyte disposal and iron recycling requires transient macrophages in the liver. Nature medicine *22*, 945-951.

Toh, S.Q., Glanfield, A., Gobert, G.N., and Jones, M.K. (2010). Heme and blood-feeding parasites: friends or foes? Parasites & Vectors *3*, 108.

Vogt, S. (2003). MAPS: A set of software tools for analysis and visualization of 3D X-ray fluorescence data sets. J Phys IV France *104*, 635-638.

White, C., Yuan, X., Schmidt, P.J., Bresciani, E., Samuel, T.K., Campagna, D., Hall, C., Bishop, K., Calicchio, M.L., Lapierre, A., *et al.* (2013). HRG1 Is Essential for Heme Transport from the Phagolysosome of Macrophages during Erythrophagocytosis. Cell Metab *17*, 261-270.

Winter, W.E., Bazydlo, L.A., and Harris, N.S. (2014). The molecular biology of human iron metabolism. Laboratory medicine *45*, 92-102.

Zhang, J., Chambers, I., Yun, S., Phillips, J., Krause, M., and Hamza, I. (2018). Hrg1 promotes heme-iron recycling during hemolysis in the zebrafish kidney. PLoS genetics *14*, e1007665.

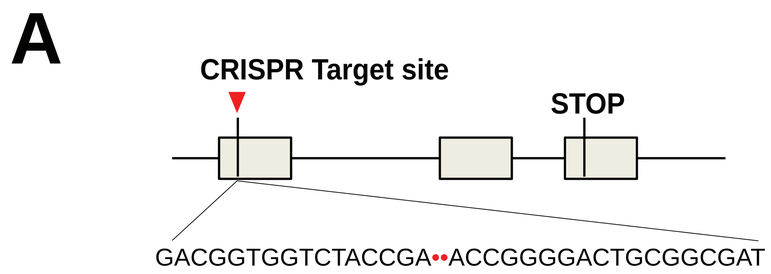

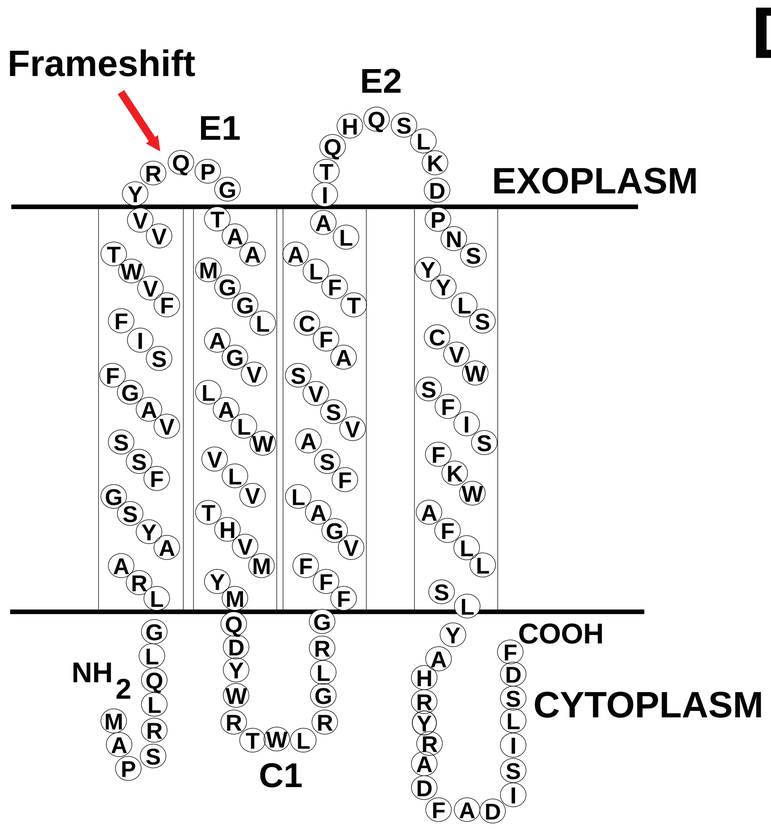

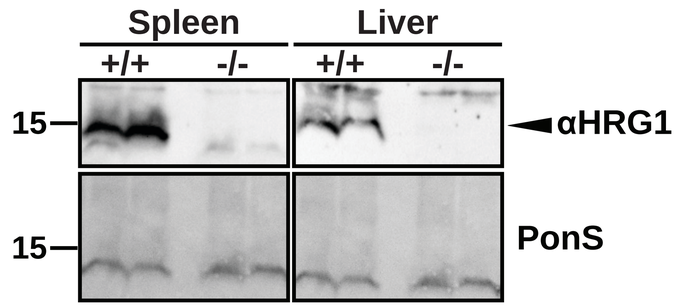

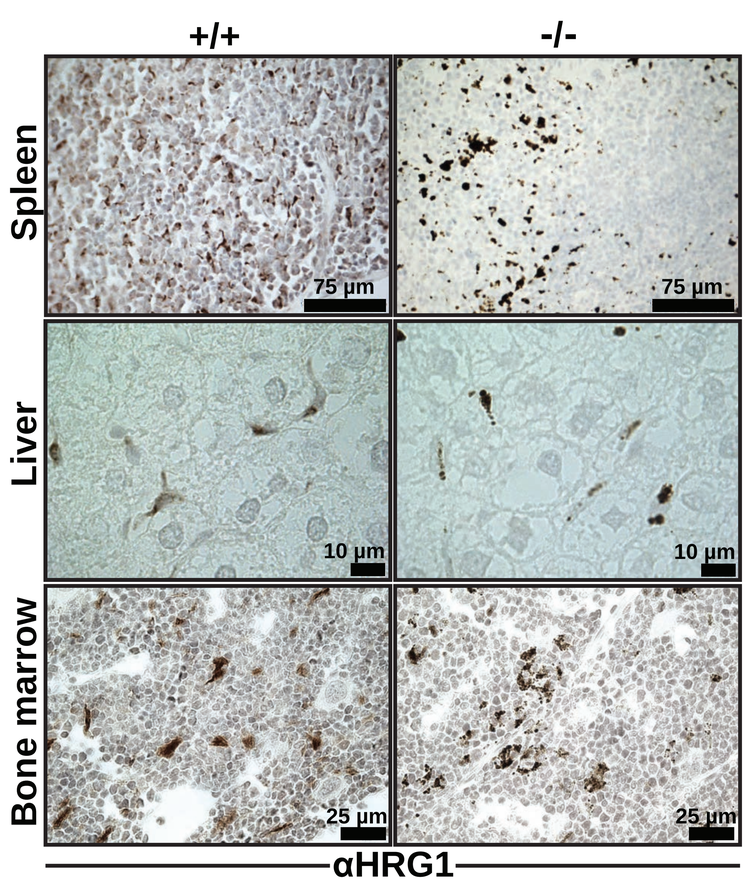

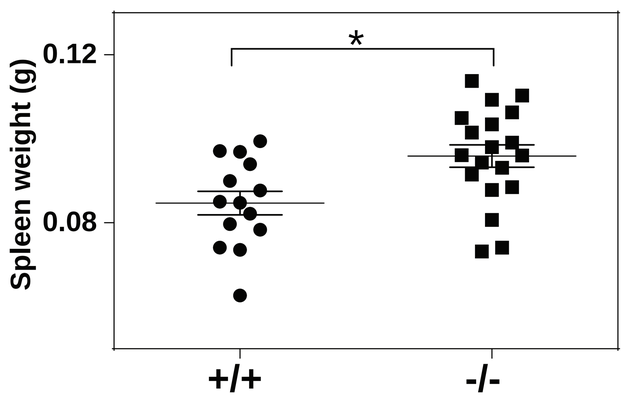

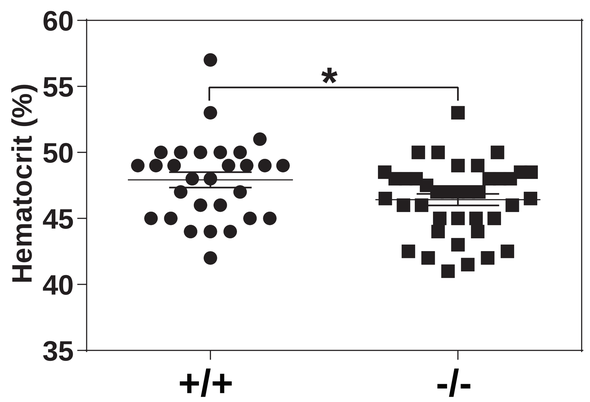

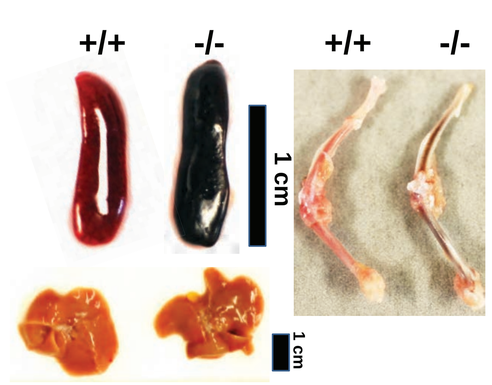

Figure 1. Reticuloendothelial tissues accumulate dark pigments in the absence of *HRG1*

A) Structure of the *SLC48A1* gene (which encodes HRG1) indicating the CRISPR target site in exon 1. **B)** Predicted topology of HRG1 protein; arrow indicates the site of the 2 basepair deletion resulting in frameshift mutation. **C)** Immunoblot analysis of membrane lysates prepared from spleens and livers of mice. Membranes were probed with anti-HRG1 antibody and then incubated with HRP-conjugated anti-rabbit secondary antibody. Each lane represents one animal. **D)** HRG1 immunohistochemistry analysis of paraffin-embedded tissue sections of mice. Tissue sections were probed with affinity-purified anti-HRG1 antibody and then incubated with HRP-conjugated anti-rabbit secondary antibody. Images shown are representative of at least 3 mice. **E-F)** Spleen wet weights and whole blood hematocrit from *HRG1*$^{+/+}$ and *HRG1*$^{-/-}$ mice. Each dot represents one mouse; mice were age (6 weeks) and sex-matched. **G)** Representative images of spleens, livers and bone marrows of age and sex-matched mice. * $p<0.05$.

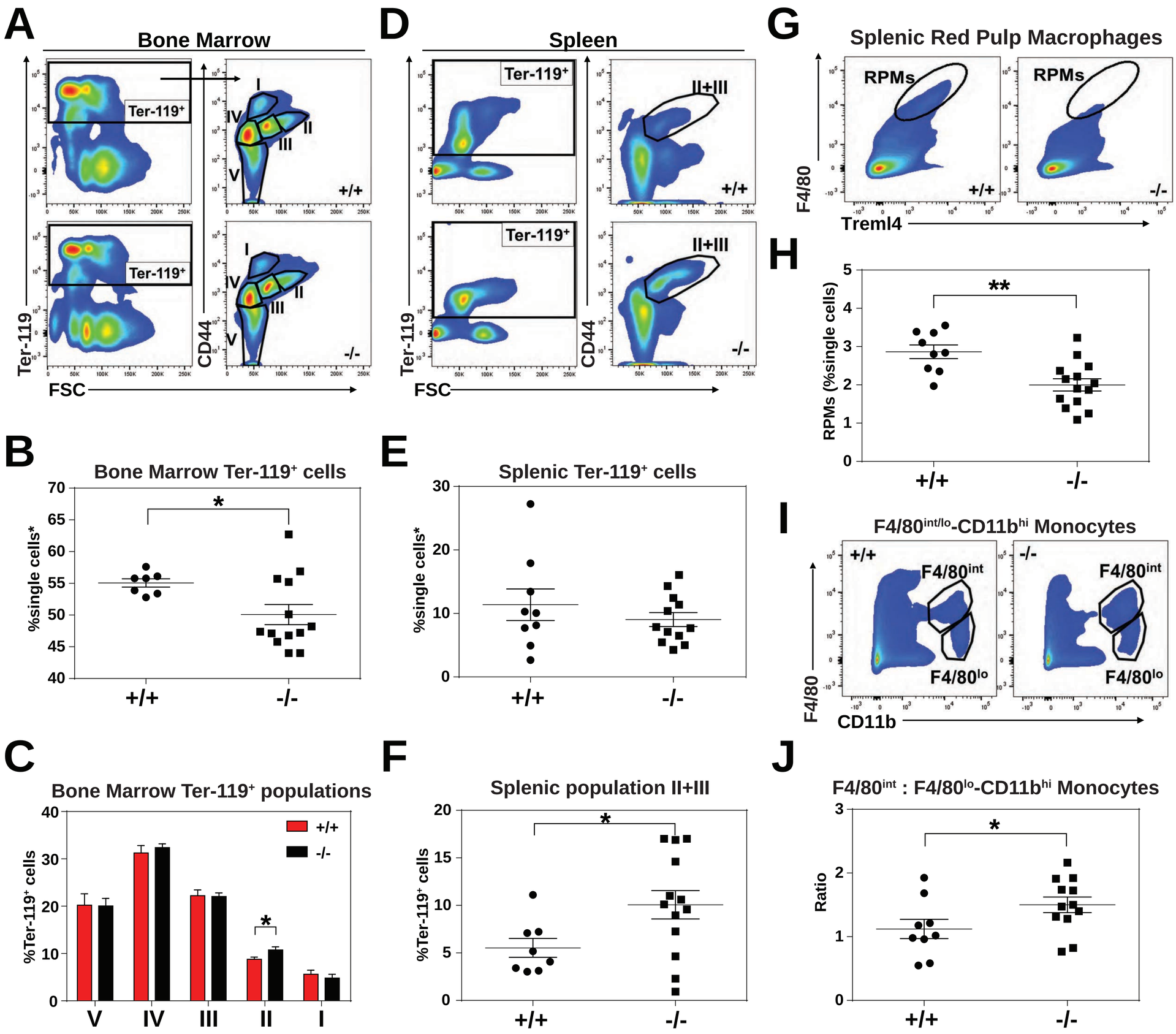

Figure 2. *HRG1*$^{-/-}$ mice exhibit extramedullary erythropoiesis with fewer mature RPMs

Gating strategy of Ter-119^{+} cells in the (**A)** bone marrow and **(D)** spleen. Quantifications of total Ter-119^{+} cells in the **(B)** bone marrow and **(E)** spleen. The %single cells* on the y-axis denote single cells that are negative for CD4/8/41, B220 and Gr-1. **C)** Quantification of subpopulations of Ter-119^{+} cells represented as a percentage of total Ter-119^{+} cells in the bone marrow (n=7-12). **F)** Quantification of populations II and III of Ter-119^{+} cells represented as a percentage of total Ter-119^{+} cells in the spleen. Gating strategy **(G, I)** and quantification **(H, J)** of **(G, H)** splenic F4/80^{hi}Treml4^{+} red pulp macrophages (RPMs) and **(I, J)** F4/80^{hi} and F4/80^{lo}-CD11b^{hi} splenic monocytes. At least 100,000 single cells were analyzed per sample. Each dot represents one mouse. **p<0.05; **p<0.01.

Figure 3. Heme accumulates within RES macrophages of *HRG1*$^{-/-}$ mice

Histochemical staining of spleen, liver and bone marrow tissue sections of *HRG1*$^{+/+}$ and *HRG1*$^{-/-}$ mice with H&E **(A)** or Perl's Prussian blue **(B).** Arrows indicate dark pigments in *HRG1*$^{-/-}$ tissues. Images shown are representative of at least 3 mice. Quantification of tissue iron **(C)** and heme **(D)** by ICP-MS and UPLC, respectively in tissues of mice fed a standard diet (n=6-17). **E)** F4/80 immunohistochemistry analysis of paraffin-embedded tissue sections of mice. Yellow arrows indicate dark pigments within F4/80-positive cells. At least 3 mice were analyzed per genotype. **F)** XFM of F4/80-positive bone marrow macrophages from *HRG1*$^{+/+}$ and *HRG1*$^{-/-}$ mice. **G)** Quantification of total cellular concentrations of indicated elements, organized by cellular abundance. **H)** ROI concentration within dark aggregates in *HRG1*$^{-/-}$ BMMs. Quantifications were measured for n=5 cells per genotype. *p<0.05; **p<0.01; ***p<0.001; ****p<0.0001.

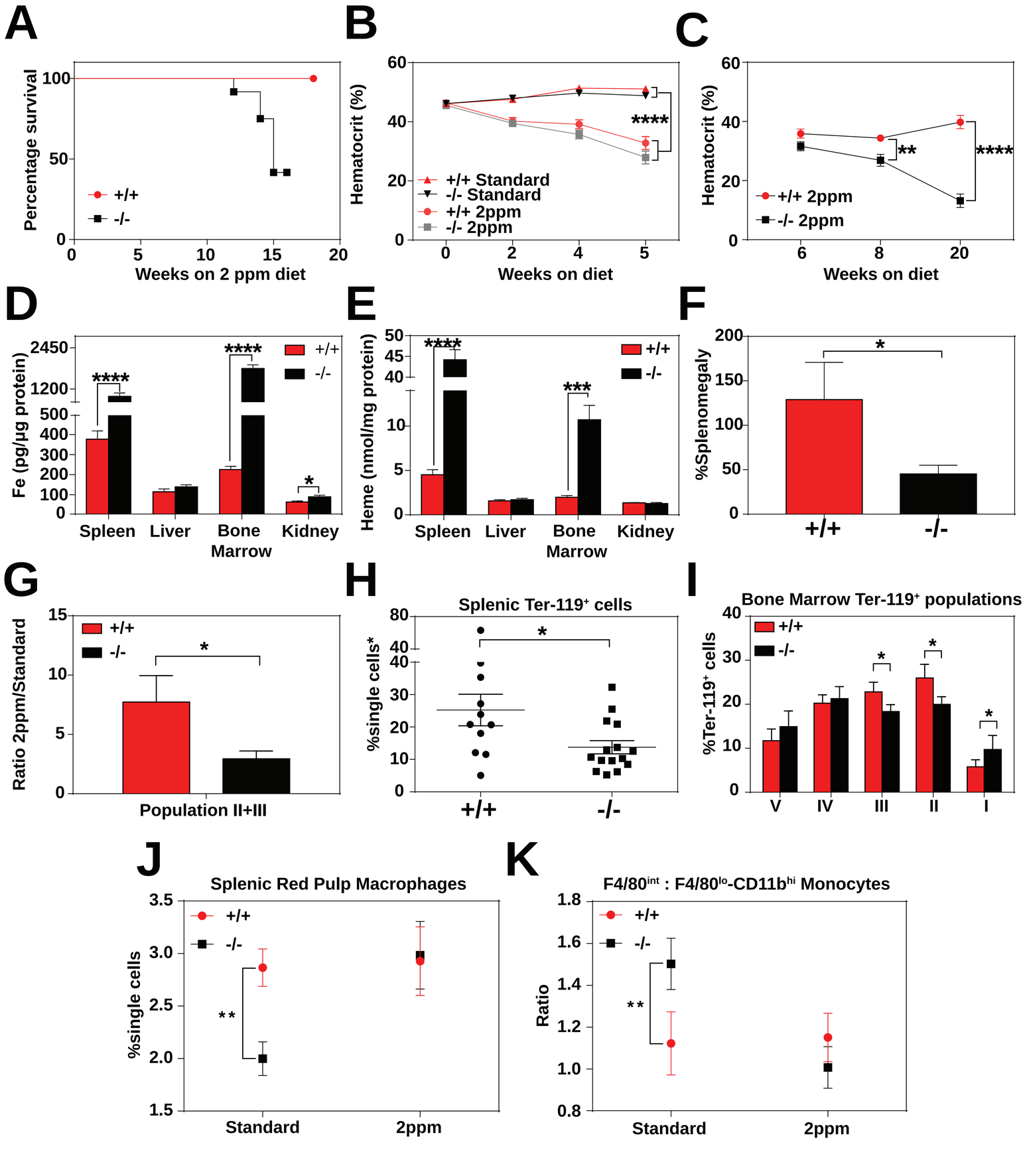

Figure 4. Dietary iron deficiency disrupts iron metabolism gene expression in *HRG1*$^{-/-}$ mice and results in lethality

A) Kaplan-Meier survival curve of *HRG1*$^{+/+}$ and *HRG1*$^{-/-}$ mice placed on a low-iron (2ppm) diet (n=15-17, both males and females). **B-C)** Hematocrits of *HRG1*$^{+/+}$ and *HRG1*$^{-/-}$ mice placed on a standard or low-iron (2ppm) diet. Mice were placed on respective diets supplemented with deionized water starting at 21 days of age (week 0) (n=9-15 for 5-week data set; n=7-11 for 20-week data set). Quantification of tissue iron **(D)** and heme **(E)** by ICP-MS and UPLC respectively, in tissues of mice fed a low-iron (2ppm) diet (n=6-17). **F)** %Splenomegaly of *HRG1*$^{+/+}$ and *HRG1*$^{-/-}$ mice calculated by the percentage of increase in average wet weight of spleens between mice on low-iron versus standard iron diets (n=9-15); **G)** Ratio of 2ppm splenic Ter-119^{+} population II+III cells to that of standard diet mice (n=8-12); **H)** Quantification of total Ter-119^{+} cells in the spleen. The %single cells* on the y-axis denote single cells that are negative for CD4/8/41, B220 and Gr-1. Each point represents one mouse. **I)** Quantification of subpopulations of Ter-119^{+} cells represented as a percentage of total Ter-119^{+} cells in the bone marrow (n=7-8); **J)** Quantifications of splenic RPMs in mice on a standard or low-iron (2ppm) diet, represented as a percentage of single cells analyzed (n=9-14). **K)** Quantification of the ratio of F4/80^{hi} to F4/80^{lo}CD11b^{hi} splenic monocytes from mice on a standard or low-iron (2ppm) diet (n= 9-15). At least 100,000 single cells were analyzed per sample. **L)** Gene expression heat map of 90 iron metabolism genes in spleens from mice on standard or low-iron (2ppm) diet. Pearson correlation was used for comparison; average linkage (n=9 per group, per genotype). *p<0.05; **p<0.01; ***p<0.001; ****p<0.0001.

Figure 5. Loss of *HRG1* produces hemozoin biocrystals within enlarged lysosomes due to impaired erythrophagocytosis

A) Experimental design of ^{59}Fe labeling and *in vivo* recycling. **B)** Quantification of ^{59}Fe retained in tissues, represented as the ratio of the amount of radioactivity within an organ to that of the entire animal. **C)** ^{59}Fe retained in differentially extracted fractions of the spleen at 96 h, represented as counts per min. Total homogenate: homogenized and proteinase-treated whole spleen; Organic: ethyl acetate extractable [^{59}Fe]heme; Aqueous: ethyl acetate non-extractable ^{59}Fe; Insoluble fraction: proteinase-insoluble fraction containing ^{59}Fe (n=4-6 across all groups and timepoints). **D)** Image of insoluble fractions before and after dissolving in buffer. **E)** Visible spectra of dissolved insoluble fractions. **F)** Powder x-ray diffraction of purified insoluble fraction from *HRG1*$^{-/-}$ spleens (red: measured data; dark blue: calculated pattern; light blue: background; green: structural plot) **G)** Chemical structure of hemozoin from *HRG1*$^{-/-}$ mice. **H)** Quantification of spenic heme by spectrophotometric measurements (n=3). **I)** Scanning electron microscopy of hemozoin isolated from Plasmodium, *HRG1*$^{-/-}$ spleen, liver, and bone marrow. **J)** Transmission electron microscopy of F4/80^{+} bone marrow and splenic macrophages from *HRG1*$^{+/+}$ and *HRG1*$^{-/-}$ mice. At least 3 cells were imaged per genotype. **K)** Confocal microscopy of bone marrow macrophages from *HRG1*$^{+/+}$ and *HRG1*$^{-/-}$ mice probed with anti-LAMP1 antibody and secondary alexa-488 antibody. Hemozoin is pseudocolored as orange. White arrow points to hemozoin-laden vesicle, yellow arrow points to non hemozoin-laden vesicle. At least 20 cells were analyzed per genotype. *p<0.05; **p<0.01.

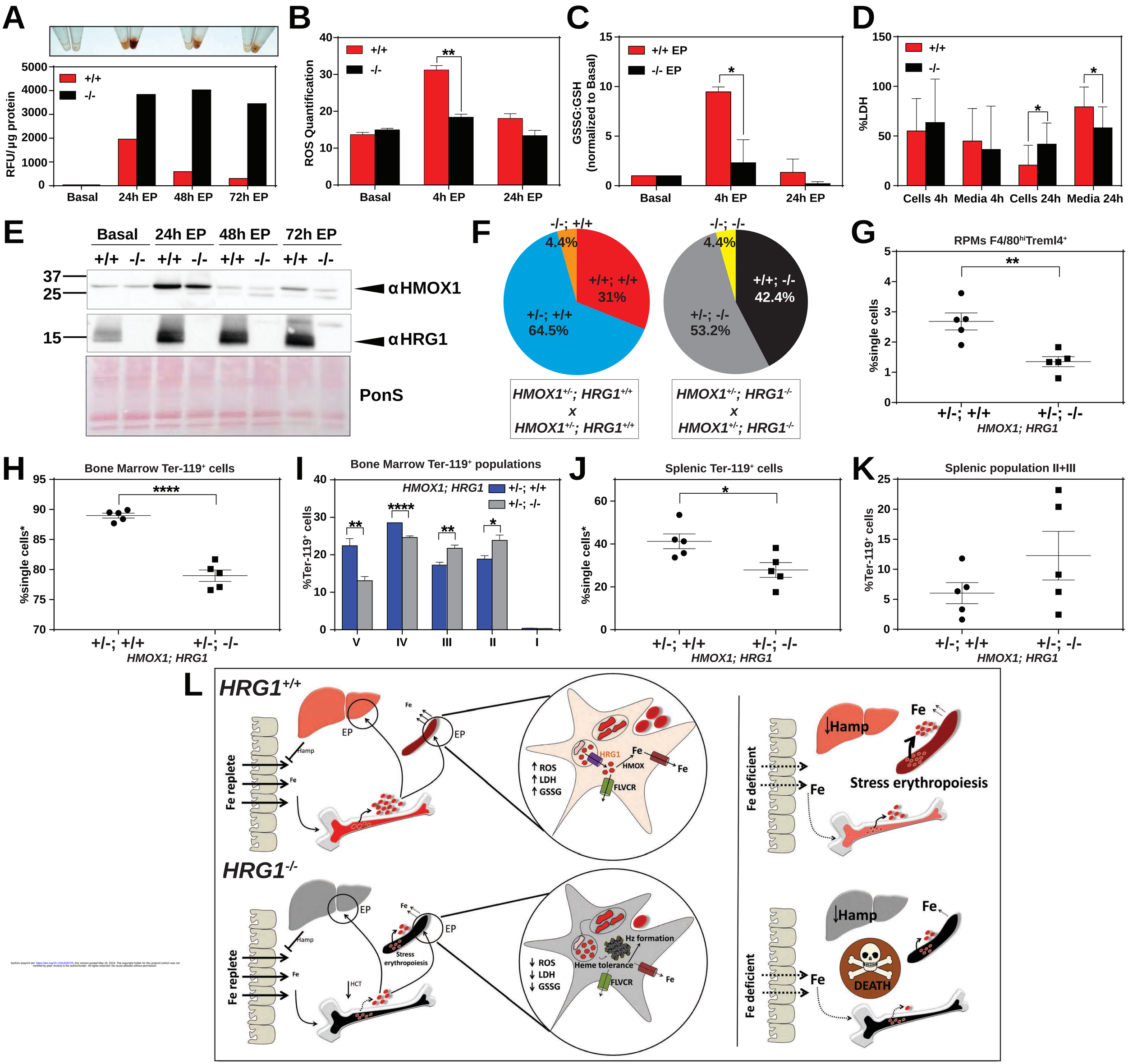

Figure 6. *HRG1* deficiency confers cellular heme tolerance during erythrophagocytosis and haploinsufficiency of *HMOX1* in *HRG1*-deficient animals causes perinatal lethality
A) Images of cell lysates and quantification of heme content in *HRG1*$^{+/+}$ and *HRG1*$^{-/-}$ BMDMs at basal (no treatment), 24 h, 48 h and 72 h post-EP (erythrophagocytosis). Results are representative of at least two experiments. **B)** Quantification of intracellular reactive oxygen species (ROS) in *HRG1*$^{+/+}$ and *HRG1*$^{-/-}$ BMDMs at basal, 4 h and 24 h post-EP. **C)** Ratio of cellular GSSG:GSH in *HRG1*$^{+/+}$ and *HRG1*$^{-/-}$ BMDMs at basal, 4 h and 24 h post-EP. Values for 4 h and 24 h are normalized to basal values. The values shown are a combination of two representative biological replicates. **D)** LDH content in cells and media of *HRG1*$^{+/+}$ and *HRG1*$^{-/-}$ BMDMs at 4 h and 24 h post-EP, represented as percentage of total LDH in cells and media. **E)** Immunoblots of HMOX1 and HRG1 protein of BMDM lysates shown in (A). **F)** Percentages of pups born of the indicated genotypes for *HMOX1*$^{+/-}$ intercrosses, either on a *HRG1*$^{+/+}$ or *HRG1*$^{-/-}$ background. **G)** Quantification of splenic RPMs in *HMOX1*$^{+/-}$*HRG1*$^{+/+}$ and *HMOX1*$^{+/-}$*HRG1*$^{-/-}$ mice by flow cytometry. **H)** Quantification of total Ter-119^{+} cells in the bone marrow. The %single cells* on the y-axis denote single cells that are negative for CD4/8/41, B220 and Gr-1. **I)** Quantification of subpopulations of Ter-119^{+} cells represented as a percentage of total Ter-119^{+} cells in the bone marrow. **J)** Quantification of total Ter-119^{+} cells in the spleen. The %single cells* on the y-axis denote single cells that are negative for CD4/8/41, B220 and Gr-1. **K)** Quantification of populations II and III of Ter-119^{+} cells represented as a percentage of total Ter-119^{+} cells in the spleen. At least 100,000 single cells were analyzed per sample. Each dot represents one mouse. Both male and female mice were analyzed in the experiments conducted in Figure 6. **L)** Proposed model for the *in vivo* and *in vitro* function of HRG1 in heme-iron recycling of RBCs under systemic iron replete and deficient conditions. *p<0.05; **p<0.01; ****p<0.0001.